

Cycles and Thermal System Integration Issues of Ultra-Micro Gas Turbines

Toshio NAGASHIMA and Koji OKAMOTO

Department of Aeronautics and Astronautics
University of Tokyo
7-3-1, Hongo, Bunkyo
Tokyo 113-8656
JAPAN

tnaga@mail.ecc.u-tokyo.ac.jp

Yves RIBAUD

ONERA DEFA
29 Avenue de la Division Leclerc, BP 72
92322 Chatillon Cedex
FRANCE

Yves.Ribaud@onera.fr

ABSTRACT

A synthesis of elementary heat balances along the gas path to establish a global energetic on the PowerMEMS type ultra-micro gas turbines (UMGT) is discussed, emphasizing, in particular, a new formulation of turbo-component performance in the presence of intense heat transfer. A potential benefit to integrate a wave rotor into UMGT system will be also presented to demonstrate the design feasibility according to numerical and experimental studies on a scaled-up model.

1 INTRODUCTION

Ubiquitous society for us in the near future will ensure individual management of energy devices for electricity, air conditioning and ground/space transport, just as we presently enjoy lap-top computers and cell phones for personal use, which all in all could profoundly expand the freedom of our social activities. The battery, though convenient and good in specific output [W/kg], is not satisfactory with respect to specific energy [W-hr/kg] for prolonged use of the above mobile info-communication devices, needless to mention about inadequate application for actuating robots and UAV propulsion. Whilst, the fuel cells, typically DMFC and PEFC, are adequate for sustainability, their specific output might remain poor and unsuitable for mobile compactness. Internal combustion engines, which are good in both specific output and energy for fuel chemical property reason, are therefore advantageous for miniaturization. In particular, gas turbines can be the first candidate due to simple and light structure, which have been well developed for aero-engines and co-generation power plants towards not only the larger output, but also the smaller according to the recent demands on distributed electricity management.

Recent advancement in developing micro gas turbines, that is, of output range of hundreds kW, is a hopeful sign to achieve further miniaturization, however, a technical data base is definitely lacking for designing ultra-micro gas turbines (UMGT), extremes of the smallest system as represented by PowerMEMS turbines, with respect to thermal, fluid dynamic and structural integrity of system components. Precise investigation and practical experience are necessary for performance prediction and improvement

in major components like compressor, turbine and combustor that require more firm knowledge about non-adiabatic and low Re number flows, fuels and mixing to result in stable micro flame, bearings and seal to sustain over-million rpm rotation, manufacture tolerance, ultra-compact motor and electric generator. A point to be stressed, therefore, may be that, though tiny in size, UMGT is an engine system of huge synthesis of thermo-fluid and combustion mechanisms, so that a step forward accuracy has to be realized to examine individual micro mechanism that will accompany profound difficulty in performing experimental measurements, thus, necessitates a new tool, most likely computer simulations, which will also play a significant role upon hardware designing and fabrication.

Another innovative aspect for UMGT system may be introduction of a new system component, typically, a wave rotor. Thermodynamic cycle to employ the latter as a topping is known prospective for aero-engines with low pressure ratio and high turbine inlet temperature, such as turboshaft and auxiliary power units, so that active work has been made at NASA GRC, including recent application for pulse detonation engines. Main interest in the wave rotor work so far aimed at application for the larger power output gas turbines, but it should be noted that working principle of wave rotors is fundamentally different from the conventional turbo-components that utilizes gas dynamic force acting upon rotors. Therefore, a potential advantage of employing wave rotors can be accentuated in difficult situation when the rotor power gets worse to be converted from gas dynamic power due to fluid viscosity, that is empirically foreseen in miniaturized turbo-components. Wave rotors become a very attractive choice amongst several UMGT system components including heat exchangers, for the improvement in performance, increasing the cycle pressure ratio and yielding also a regenerative effect. A wave rotor topped UMGT cycle is thus worth investigating in detail, which will lead to enlarge the sphere of research and technical activity for realizing a new mobile power conversion system.

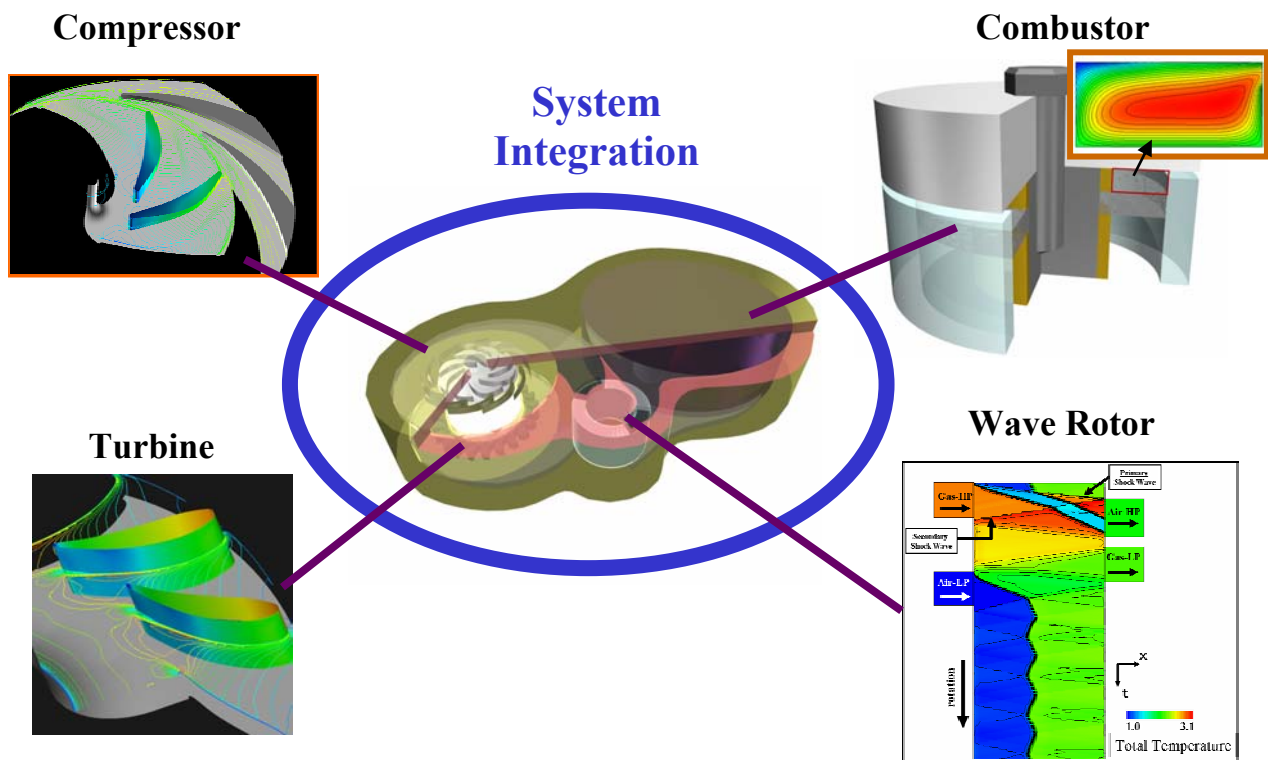


Figure 1: Innovative Miniature Gas Turbine System.

The purpose of this study, therefore, is twofold, in the first, to establish a methodology for precise consideration, at UMGT design base, upon global energetic links between localized heat transfer to

eventually comprise a total heat balance, whilst, in the second, to explain about wave rotors, in particular, towards miniaturization in application for UMGH topping cycle.

In the first part, the best suited demonstration is provided by modelling precise Power-MEMS turbines proposed by MIT [1]. Heat transfer by forced internal convection, material conduction, outside radiation and natural convection is amplified in these tiny engines. In particular, compressor and turbine behave also like heat exchangers and this for three reasons: first with small Reynolds numbers encountered because of small scale, gas convective heat transfer coefficient increases by a factor of the order of three compared to usual turbo-machines, next the temperature difference between gas and material is important because of low value of Biot number, typically of the order of 0.01 for SiC in use, finally the specific speed of the turbo-machines is not optimum so the surface effects like convective heat transfer are increased.

In the second part, a question is raised concerning a penalty in compactness and weight by attaching a wave rotor, which needs to be answered by counting the gains to compensate the penalty. It will be the system integrity that matters, in other words, to match the wave rotor size compatible with the engine core and to achieve significant reduction in fuel consumption to realize the least system volume including a fuel tank. It will be a very ambitious technological challenge, by installing a micro wave rotor, to dispense with Power-MEMS combustor and heat exchanger altogether.

The answer to a simple but important question ‘is Power-MEMS turbine feasible?’ is yet not clear, in terms of fabrication of components and system integration from aero-thermodynamic, mechanical, material and structural points of view. It remains to be very difficult to answer, since there exists no data available for producing and testing such millimetre size turbo-machinery.

2 HOT BUTTON THERMODYNAMIC MODEL

A key attempt in the present modelling is **to separate aerodynamic losses in the turbo-components and heat transfer**, which both contribute to entropy rise, because heat transfer is, for a large part, function of the architecture and material choices whereas aerodynamic losses maybe well handled by careful treatment for low Reynolds numbers flows.

2.1 Micro Turbine Model

2.1.1 Isotemperature of the Micro Turbine

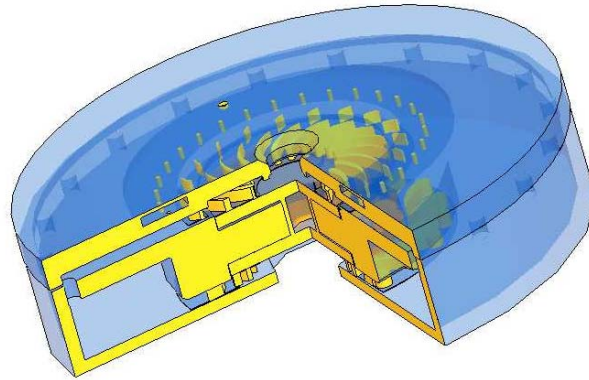
As the mean Biot number (internal convective heat transfer over material conduction) in the engine is of the order of 1 – 3 percent with SiC, the hypothesis of constant temperature in the material is met. So it is appropriate to consider that there are two (or three) levels of temperature, one (or two) for the rotor(s), the other for the stator. In fact there are two levels of temperature if the rotating disc is common to compressor and turbine, and three if compressor rotor and turbine rotor are connected by a shaft which impedes thermal conduction.

2.1.2 Heat Transfer in the Micro Turbine

Figure 2 presents a scheme of possible convective and radiative heat transfer between gas (or the outside) and material. We can distinguish it as follows: (Table 1)

- Convective heat transfer between the internal fluid and the stator (transfer 2, 3, 4, 6, 10, 11, 12, 13)
- Convective heat transfer between the internal fluid and the rotor (transfer 8, 9)
- Convective heat transfer between the stator and the rotor (transfer 5, 5' and 7 in the interdisc cavities)

- Convective and radiative heat transfer between the stator and the outside (transfer 1)
- The conduction in the material is implicit



Dessin réalisé par des Elèves de l'Ecole Supérieure d'Electronique d'Angers

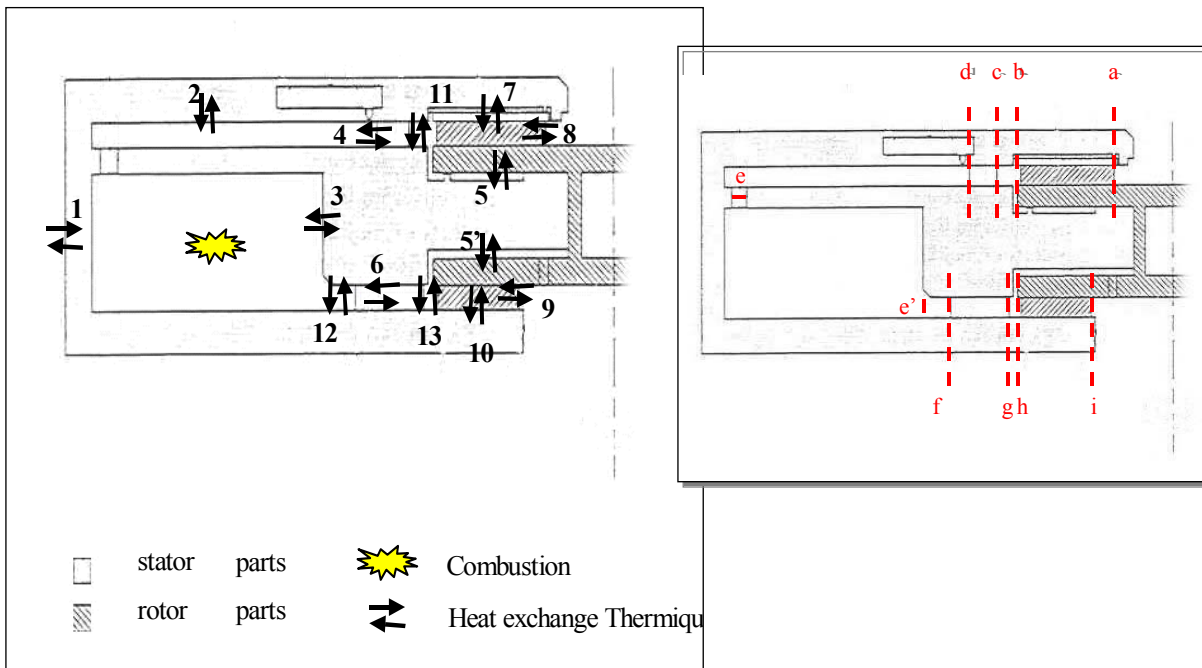


Figure 2: Heat Transfer Scheme in the Micro Turbine.

Table 1: Heat Transfer List

1	Outside ⇒ stator
2	Fluid ⇒ stator, mixing channel
3	Fluid ⇒ stator, combustion chamber
4	Fluid ⇒ stator, vaned diffuser
5	Rotor/stator ⇒ rear compressor disc
5'	Rotor/stator ⇒ rear turbine disc
6	Fluid ⇒ stator, IGV
7	Rotor/stator ⇒ front compressor disc
8	Fluid ⇒ rotor, compressor rotor
9	Fluid ⇒ rotor, turbine rotor
10	Fluid ⇒ stator, turbine stator(rotor shroud)
11	Fluid ⇒ stator, vaneless diffuser
12	Fluid ⇒ stator vaneless space, upstream IGV
13	Fluid ⇒ stator, vaneless space, upstream of the turbine rotor

a	The compressor rotor inlet
b	The compressor rotor exit
c	The vaned diffuser inlet
d	The diffuser exit/inlet of the premixing channel
e	Exit of the premixing channel/combustion inlet
e'	Combustion chamber exit
f	IGV inlet
g	IGV exit
h	Turbine rotor inlet
i	Turbine rotor exit

Remark: In this presentation, the sign 1, 2, 3 is related to a given heat transfer and the sign a, b, c is associated with a given section.

2.2 Aerodynamic Polytropic Efficiency

2.2.1 Compressor

For adiabatic case, a well known relation between total pressures and total temperatures is:

$$\frac{T_{ib}}{T_{ia}} = \left(\frac{P_{ib}}{P_{ia}} \right)^{\left(\frac{\gamma_{air}-1}{\gamma_{air} \eta_{pol\ comp}} \right)} \quad (1)$$

(in this study, the total pressure P_i is supposed to be constant downstream of the rotor)

For non-adiabatic case, aerodynamic losses δf^+ is also compared to the mechanical work dW given to compressor:

$$dW(1 - \eta_{pol\ comp}) = \delta f^+ \quad (2)$$

with this definition $\eta_{pol\ comp}$ is still a measurement of the aerodynamic losses only.

In order to calibrate the heat transfer in compressor rotor, a parameter is introduced:

$$\lambda_{comp} = -\frac{Q_8}{P_{comp}} \quad (3)$$

where P_{comp} is the power given to the compressor and Q_8 the heat transfer from the main fluid to the rotor.

The power given to compressor can be calculated from:

$$P_{comp} = \dot{m}_{air} C_{p_{air}} T_{ia} \left[\left(\frac{P_{ib}}{P_{ia}} \right)^{\frac{r_{air}}{C_{p_{air}} \eta_{pol \ comp}}} - 1 \right] \quad \text{for adiabatic} \quad (4)$$

$$P_{comp} = \left[\frac{\dot{m}_{air} C_{p_{air}} T_{ia}}{1 + \lambda_{comp}} \right] \left[\left(\frac{P_{ib}}{P_{ia}} \right)^{\frac{r_{air}(1+\lambda_{comp})}{C_{p_{air}} \eta_{pol \ comp}}} - 1 \right] \quad \text{for non-adiabatic} \quad (5)$$

where \dot{m}_{air} is the air mass flow rate.

The power given to compressor (after having deduced the disc friction power) is calculated from the second Euler theorem

$$P_{comp} = \dot{m}_{air} \omega r_b V_{tb} \quad (6)$$

Even with a small change of the absolute tangential velocity V_{tb} due to heat transfer, this power is nearly constant. So when the internal fluid in the rotor is heated by the walls then the pressure ratio is reduced:

$$\Pi_C = \frac{P_{ib}}{P_{ia}} = \left(\frac{T_{ib}}{T_{ia}} \right)^{\frac{C_{p_{air}} \eta_{pol \ comp}}{r_{air}(1+\lambda_{comp})}} \quad (7)$$

2.2.2 TURBINE

The approach is the same as for the preceding paragraph:

$$\lambda_{turb} = -\frac{(Q_9 + Q_{10})}{P_{turb}}, \quad (P_{turb} > 0) \quad (8)$$

and the relation between total temperature and pressure is given by:

$$\frac{T_{ii}}{T_{ih}} = \left(\frac{P_{ii}}{P_{ih}} \right)^{\frac{(\gamma_{gaz \ brulés} - 1) \eta_{pol \ turb}}{\gamma_{gaz \ brulés}}} \quad \text{for adiabatic} \quad (9)$$

$$\frac{T_{ii}}{T_{ih}} = \left(\frac{P_{ii}}{P_{ih}} \right)^{\frac{(\gamma_{gaz \ brulés} - 1) \eta_{pol \ turb} (1 - \lambda_{turb})}{\gamma_{gaz \ brulés}}} \quad \text{for non-adiabatic} \quad (10)$$

The power delivered by turbine is given by:

$$P_{turb} = \dot{m}_{gaz\ br\ul{e}s} C_{p_{gaz\ br\ul{e}s}} T_{ih} \left[1 - \left(\frac{P_{ii}}{P_{ih}} \right)^{\frac{r_{gaz\ br\ul{e}s} \eta_{pol\ turb}}{C_{p_{gaz\ br\ul{e}s}}}} \right] \quad \text{for adiabatic} \quad (11)$$

$$P_{turb} = \frac{\dot{m}_{gaz\ br\ul{e}s} C_{p_{gaz\ br\ul{e}s}} T_{ih}}{1 - \lambda_{turb}} \left[1 - \left(\frac{P_{ii}}{P_{ih}} \right)^{\frac{r_{gaz\ br\ul{e}s} \eta_{pol\ turb} (1 - \lambda_{turb})}{C_{p_{gaz\ br\ul{e}s}}}} \right] \quad \text{for non-adiabatic} \quad (12)$$

At the design point, the exit moment of momentum vanishes so the turbine power is evaluated from:

$$P_{turb} = \dot{m}_{gaz\ br\ul{e}s} \omega r_h V_{th} \quad (13)$$

Instead of using the aerodynamic polytropic efficiency above, Gong [4] suggests an extension of the compressor isentropic efficiency.

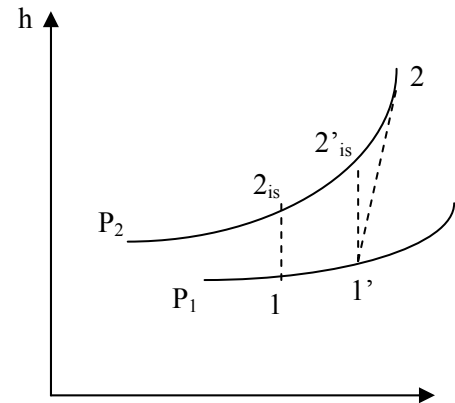
The conditions used in the following formula are stagnation ones. The conditions 1 and 2 correspond respectively to the compressor rotor inlet and exit.

In the first step, an assumption is that all the heating of the flow by the walls in the rotor takes place at the inlet:

$$C_p(T_1' - T_1) = Q \quad \text{or}$$

$$\boxed{T_1 / T_1' = 1 / (1 + Q_H) \quad \text{with } Q_H = Q / (C_p T_1) \quad (a)}$$

Q_H represents the non dimensional heat transfer between the walls and the flow in the compressor rotor.



enthalpy/entropy diagram

With this assumption, the flow between 1' and 2 is adiabatic, the corresponding isentropic efficiency is η_{is} .

The rotor compressor ratio is then given by:

$$\boxed{\pi = p_2 / p_1 = [\eta_{is} (T_2 - T_1') / T_1' + 1]^{\gamma / (\gamma - 1)}} \quad (b)$$

or if the non dimensional mechanical work is introduced,

$$\boxed{\bar{W} = W / (C_p T_1) = (T_2 - T_1') / T_1} \quad (c)$$

finding:

$$\boxed{\pi = p_2 / p_1 = [\eta_{is} \bar{W} / (1 + Q_H) + 1]^{\gamma / (\gamma - 1)}} \quad (d)$$

but the real efficiency of the rotor is given by:

$$\eta_{\text{real}} = C_p(T_{2\text{is}} - T_1)/W = \eta_{\text{is}}/(1+Q_H) \quad (\text{e})$$

If the flow were adiabatic, with the same work \bar{W} , one would obtain a better pressure ratio:

$$\pi_{\text{ad}} = [\eta_{\text{is}} \bar{W} + 1]^{\gamma/(\gamma-1)} \quad (\text{f})$$

by eliminating \bar{W} between (d) and ((f) we obtain a lower pressure ratio:

$$\pi = [(\pi_{\text{ad}})^{(\gamma-1)/\gamma} - 1]/(1+Q_H) + 1]^{\gamma/(\gamma-1)} \quad (\text{g})$$

These extended efficiency relations are strictly valid only for the compressor and turbine rotors. In the compressor diffuser, the heat transfer lowers a very little amount the total pressure, depending of the local Mach numbers. While the total temperature rise in the diffuser seems beneficial, as shown in the applications, cooling the material is finally detrimental to the thermodynamic cycle, because heat transfer in other parts as for example in the turbine NGV of the microturbine is modified in the wrong way. Heat transfer in the turbine NGV which is very important, for a given exit Mach number, lowers a lot the moment of momentum at the rotor turbine inlet, which is also detrimental to the power given by the turbine rotor. It has to be finally mentioned that heat transfer increases, but by a very little factor, the total pressure in the NGV, depending on the local Mach numbers in this cascade.

2.3 Quantitative Heat Transfer Study

The calculations are first performed in the adiabatic situation which is not realistic but constitutes a good reference, and then in the real situation.

2.3.1 Aerodynamic and Thermodynamic Calculations

Input:

air standart conditions

air mass flow m_{air} ,

rotor angular velocity ω ,

rotor aerodynamic polytropic efficiencies

compressor rotor work factor $\mu^c \sim 0.8 = v_{\text{tb}}/\omega r_b$

maximum temperature in the combustion chamber $T_{\text{chambre}} = T_e \sim 1600\text{K}$ for SiC

geometry of the microturbine

type of fuel

Section (a): Compressor Rotor Inlet

Equations: mass flow and moment of momentum equations \Rightarrow velocity triangle, aerodynamic conditions.

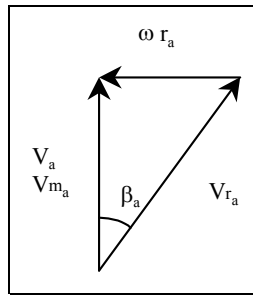


Figure 3: Velocity Triangle, Compressor Rotor Inlet.

Section (b): Compressor Rotor Exit

Equations: work coefficient $\mu^c = v_{tb}/\omega r_b$
 energy equation with heat transfer between (a) and (b)
 mass flow conservation

velocity triangle
aerodynamic conditions

the total temperature ratio and the total pressure ratio are connected by the relation:

$$T_{ib} = T_{ia} \left(\frac{P_{ib}}{P_{ia}} \right)^{\frac{(\gamma_{air}-1)(1+\lambda_{comp})}{\gamma_{air} \eta_{pol, comp}}}$$

($\lambda_{comp} = 0$ for adiabatic flows)

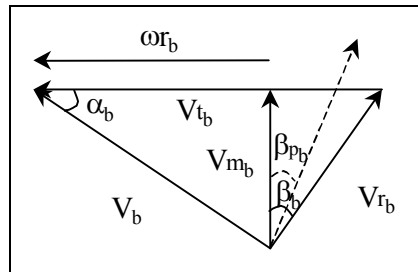


Figure 4: Velocity Triangle, Compressor Rotor Exit.

Sections (c), (d), (e), (e'), (f): Diffuser Inlet, Diffuser Outlet, Combustor Inlet, Combustor Outlet, NGV Inlet

Equations: moment of momentum equation or flow angle condition
 energy equation with heat transfer
 mass flow conservation
 aerodynamic losses

aerodynamic
conditions

Sections (g), (h), (i): NGV Exit, Turbine Rotor Inlet, Turbine Rotor Outlet

Equations: moment of momentum equation or flow angle condition

energy equation with heat transfer

mass flow conservation

aerodynamic losses

→ aerodynamic conditions

Between (g) and (h): v_{th} must be calculated before.

Between (h) and (i):

The total pressure in (i) is the ambient one

The total temperature in (i) is given by:

$$T_i = T_{ih} \left(\frac{P_i}{P_{ih}} \right)^{\frac{(\gamma_{\text{gaz brûlés}} - 1) \eta_{\text{pol turb}} (1 - \lambda_{\text{turb}})}{\gamma_{\text{gaz brûlés}}}}$$

The tangential velocity at the turbine rotor inlet is given by the second Euler theorem which is a particular form of the energy conservation theorem. With no exhaust residual vortex, this gives:

$$V_{th} = \frac{Cp_{\text{gaz brûlés}} (T_{ih} - T_i) - \frac{Q_9 + Q_{10}}{\dot{m}_{\text{gaz brûlés}}}}{\omega r_h}$$

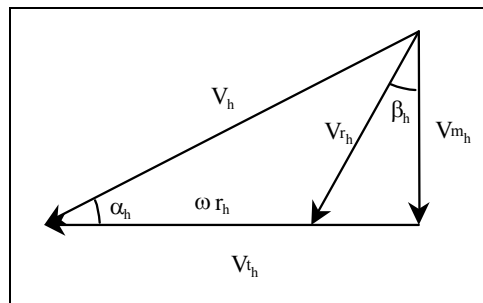


Figure 5: Velocity Triangle, Turbine Rotor Inlet.

Power Calculations

The compressor power is given by:

$$P_{comp} = \dot{m}_{air} \omega r_b V_{tb} \quad (14)$$

The turbine one by (assuming no residual vortex at design):

$$P_{turb} = \dot{m}_{\text{gaz brûlés}} \omega r_h V_{th} \quad (15)$$

and the net one by:

$$P_{mec} = P_{turb} - P_{comp} \quad (16)$$

For the useful power, the disc friction power $C_f \cdot \omega$ needs to be subtracted.

2.3.2 Non-Adiabatic Micro Turbine Calculations

Heat Transfer Evaluation

The internal convective heat transfer from the fluid to the stator and to the rotor is defined by:

$$Q_j = h_j S_j (T_{s_j} - T_{stator}) \quad j = 2, 3, 4, 5, 5', 6, 7, 10, 11, 12, 13$$

$$Q_j = h_j S_j (T_{s_j} - T_{rotor}) \quad j = 8, 9$$

where T_{s_j} is the mean fluid static temperature at the station j of the micro turbine where some heat transfer takes place.

The calorific power exchanged with outside Q_1 is written like this:

$$Q_1 = h_{ext} S_{ext} (T_{air} - T_{stator}) + \varepsilon_{si} \sigma S_{ext} (T_{air}^4 - T_{stator}^4) \quad (17)$$

Evaluation has to be made for the exchange surfaces S_j , the mean static fluid temperatures T_{s_j} and the heat transfer coefficients h_j ; so the aerothermal values in these sections (mass per unit volume, temperature, pressure, velocity) must be first calculated.

Input for Surface S_j Calculations

To determine the T_{s_j} temperatures, first the aerothermal conditions in the micro-turbine have to be known.

In particular, the total temperatures are obtained from the resolution of the system described in the following paragraphs.

Calculation of the Convective Heat Exchange Coefficients h_j

The convective heat exchange coefficients are calculated with the following formula:

$$h_j = \frac{Nu_j \lambda_j}{L_j} \quad \text{where } \lambda_j \text{ is given by: } \lambda_j = \frac{\mu_j C p_j}{Pr}$$

where Pr is the Prandtl number which value, generally admitted for the air, is: $Pr = 0,7$.

To obtain the convective heat exchange coefficients, calculations have to be made for μ_j , Nu_j and L_j at each of the considered heat transfers, that is at each of the parts of the micro-turbine.

For the h_{ext} coefficient, it is chosen between 10 to 300W / m²K. In fact it is generally chosen equal to 10W / m²K.

Calculation of the Dynamic Viscosity μ_j

The μ_j are given by the Sutherland formula: $\mu_j = \mu_0 \left(\frac{T_{s_j}}{273} \right)^{\frac{3}{2}} \left(\frac{273 + C}{T_{s_j} + C} \right)$

where: $C_{air} = 110,4 K$ $\mu_0 = 1,711.10^{-5}$

Calculation of the Nusselt Numbers Nu_j

For convective exchanges in the rotor/stator cavities (5,5',7), Nu formulae are given by Owen and al. [5], whence two Nusselt numbers are given, the first one for the rotor side and the other for the stator side:

$$Nu_{rotor} = 0,675 Re_{\phi}^{0,5} \qquad Nu_{stator} = 0,364 Re_{\phi}^{0,5}$$

where Re_{ϕ} , the rotating Reynolds number, is given by: $Re_{\phi} = \frac{\rho \omega r_{disc}^2}{\mu}$

For heat transfers 2, 3, 4, 6, 8, 9, 10, 11, 12 and 13, the Nusselt number is a function of the Reynolds number and the Prandtl number. Then, the well-known convective formulae are used:

$$Nu_j = 0,664 Pr^{\frac{1}{3}} Re_j^{\frac{1}{2}} \qquad (18) \qquad \text{Laminar flat plate}$$

$$Nu_j = 0,0366 Pr^{\frac{1}{3}} Re_j^{\frac{4}{5}} \qquad (19) \qquad \text{Turbulent flat plate}$$

$$Nu = 7,6 \qquad (20) \qquad \text{Laminar duct (} Re \leq 2000 \text{)}$$

$$Nu_j = 0,023 Pr^{\frac{2}{5}} Re_j^{\frac{4}{5}} \qquad (21) \qquad \text{Turbulent duct (} Re \geq 2000 \text{)}$$

This model of flat plates can be used only in the parts of the micro-turbine where the boundary layers developing on the internal walls of the micro-turbine do not join. Indeed, considering the dimensions of the micro-turbine, the boundary layers can join themselves, for example in the mixing or in the vaneless channels before diffuser or NGV.

For each configurations the Excel software operates automatically the choice between these formulae by determining, for each of the parts of the micro-turbine, the value of the Reynolds number, as well as the thickness of the boundary layers.

For the heat transfer in combustion chamber, the model used is the flat plate one.

Thickness of the Boundary Layers

For laminar flows, the boundary layers knowledge is realised thanks to the following formula:

$$\frac{\delta_j}{x_j} = 4,96 Re_j^{-0,5}$$

where x_j is the boundary layer length from the leading edge.

This calculation is conducted in most of the parts of the micro-turbine, that is successively in the rotor of the compressor, in the vaneless diffuser, in the vaned diffuser, in the mixing channel, in the vaneless channel between the combustion chamber and the NGV, in the NGV, in the vaneless space between the NGV and the turbine rotor, and in the turbine rotor; it corresponds to the heat transfers 2, 4, 6, 8, 9, 10, 11,

12 and 13. On the other hand, to simplify, it is supposed in this study that the boundary layers thicken constantly. So the boundary layer which was growing in a part of the micro-turbine continues to grow in the following part.

It keeps true even in the case where the fluid comes from a rotating part to a fixed part, for example it is the case between the compressor and the diffuser. Nevertheless when the fluid crosses the combustion chamber, it was supposed that there is no conservation of the boundary layer thickness. Because of the previous hypothesis, at a given step of the micro-turbine, the boundary layer length x_j corresponds to the sum of the lengths l_j along which the boundary layer was able to develop in the “previous” parts of the micro-turbine.

For compressor and turbine rotors, l_j is taken equal to the length of a blade. For the diffuser and the NGV, l_j represents the length of a streamline. For the vaneless channel and the mixing channel, l_j represents their respective length.

Reynolds Numbers Calculation

To determine the various Nusselt numbers, it is necessary to determine first the Reynolds numbers at each station of the micro-turbine. It can be obtained by:

$$Re_j = \frac{\rho_j V_j L_j}{\mu_j} \quad \text{and the rotation Reynolds number is given by: } Re_\phi = \frac{\rho \omega r_{disque}^2}{\mu}$$

Calculation of the Characteristic Length L_j

L_j is the characteristic length of the indicated transfer j ; its calculation depends on this heat transfer and thus on the part of the micro-turbine.

For the regions where the boundary layers are separate, L_j is taken as the longitudinal length of establishment of the boundary layer l_j . For those where the boundary layers are joined, L_j is taken as the hydraulic diameter. The Excel software chooses automatically the adapted length by determining the boundary layer thickness.

Energy Balance

The following equations system corresponds to energy balance in the whole microturbine

$$\left\{ \begin{array}{l} \sum_j h_j S_j (T_{s_j} - T_{stator}) + h_{ext} S_{ext} (T_{air} - T_{stator}) + \varepsilon_{si} \sigma S_{ext} (T_{air}^4 - T_{stator}^4) = 0 \quad \text{stator balance} \\ j = 2, 3, 4, 5, 5', 6, 7, 10, 11, 12, 13 \\ \\ \sum_j h_j S_j (T_{s_j} - T_{rotor}) - \sum_k h_k S_k (T_{s_k} - T_{stator}) = 0 \quad \text{rotor balance} \\ j = 8, 9 \quad k = 5, 5', 7 \\ \\ \dot{m}_{air} C_{p_{air}} (T_{ib} - T_{ia}) = \omega r_b V_{tb} - h_8 S_8 (T_{s_8} - T_{rotor}) \quad \text{fluid in the compressor rotor} \\ \\ \dot{m}_{air} C_{p_{air}} (T_{ic} - T_{ib}) = -h_{11} S_{11} (T_{s_{11}} - T_{stator}) \quad \text{fluid in the vaneless diffuser} \\ \\ \dot{m}_{air} C_{p_{air}} (T_{id_{avinj}} - T_{ic}) = -h_4 S_4 (T_{s_4} - T_{stator}) \quad \text{fluid in the vaned diffuser} \\ \\ (\dot{m}_{air} + \dot{m}_{comb}) C_{p_{prémélange}} (T_{ie} - T_{id_{apinj}}) = -h_2 S_2 (T_{s_2} - T_{stator}) \quad \text{fluid in the premixing region} \\ \\ (\dot{m}_{air} + \dot{m}_{comb}) C_{p_{gaz brûlés}} (T_{ie'} - T_{ie}) = \dot{m}_{comb} \eta_{comb} PCI_{H_2} - h_3 S_3 (T_{s_3} - T_{stator}) \quad \text{fluid in the combustor} \\ \\ (\dot{m}_{air} + \dot{m}_{comb}) C_{p_{gaz brûlés}} (T_{if} - T_{ie'}) = -h_{12} S_{12} (T_{s_{12}} - T_{stator}) \quad \text{fluid upstream of the NGV} \\ \\ (\dot{m}_{air} + \dot{m}_{comb}) C_{p_{gaz brûlés}} (T_{ig} - T_{if}) = -h_6 S_6 (T_{s_6} - T_{stator}) \quad \text{fluid in the NGV} \\ \\ (\dot{m}_{air} + \dot{m}_{comb}) C_{p_{gaz brûlés}} (T_{ih} - T_{ig}) = -h_{13} S_{13} (T_{s_{13}} - T_{stator}) \quad \text{fluid in the turbine vaneless space} \\ \\ (\dot{m}_{air} + \dot{m}_{comb}) C_{p_{gaz brûlés}} (T_{ii} - T_{ih}) = -\omega r_h V_{th} - h_{10} S_{10} (T_{s_{10}} - T_{stator}) - h_9 S_9 (T_{s_9} - T_{rotor}) \quad \text{fluid in the turbine rotor} \end{array} \right.$$

with: $T_{ie'} = T_{comb}$, $T_{ia} = T_{air}$, $T_{id_{avinj}} = \frac{\dot{m}_{air} C_{p_{air}} T_{id_{avinj}} + \dot{m}_{comb} C_{p_{comb}} T_{inj}}{\dot{m}_{air} C_{p_{air}} + \dot{m}_{comb} C_{p_{comb}}}$

The unknowns of the system are temperatures T_{stator} et T_{rotor} , the total temperatures T_{it} for l [(b), (c), (d), (e), (f), (g), (h), (i)], and the fuel flow rate \dot{m}_{comb} , with T_{sj} for j [2, 3, 4, 5, 5', 6, 7, 8, 9, 10, 11, 12, 13] given from total temperatures and Mach numbers.

To do the resolution of the system, this one is linearised for T_{stator} and \dot{m}_{comb} .

Then the system is written under the following matrix shape: $AX = B$.

Once written matrix A and B, the resolution is obtained by: $X = A^{-1}B$.

The loop used for the linearisation of the system is repeated until convergence.

Once known the total temperatures T_{it} , then the calculation of the static temperatures is performed and the temperatures T_{sj} are determined. The powers exchanged with the heat transfers can be performed when the temperatures T_{sj} , the coefficients of exchanges h_j and the surfaces of exchanges S_j are known.

Calculation of Compression and Expansion Ratios

$$\Pi_C = \frac{P_{ib}}{P_{ia}} = \left(\frac{T_{ib}}{T_{ia}} \right)^{\frac{C_{pair} \eta_{pol comp}}{\gamma_{air} (1 + \lambda_{comp})}} \quad (22)$$

$$\Pi_D = \frac{P_{ih}}{P_{ii}} = \left(\frac{T_{ih}}{T_{ii}} \right)^{\frac{C_{pgaz} \eta_{brólés}}{\gamma_{gaz} \eta_{pol turb} (1 - \lambda_{turb})}} \quad (23)$$

An iteration loop is laid in order to obtain $\Pi_C = \Pi_D$ after good calibration of v_{th} .

Calculation Chart

The non-adiabatic chart is listed on the following page and the adiabatic and non-adiabatic results for the original 1cm diameter microturbine are then presented.

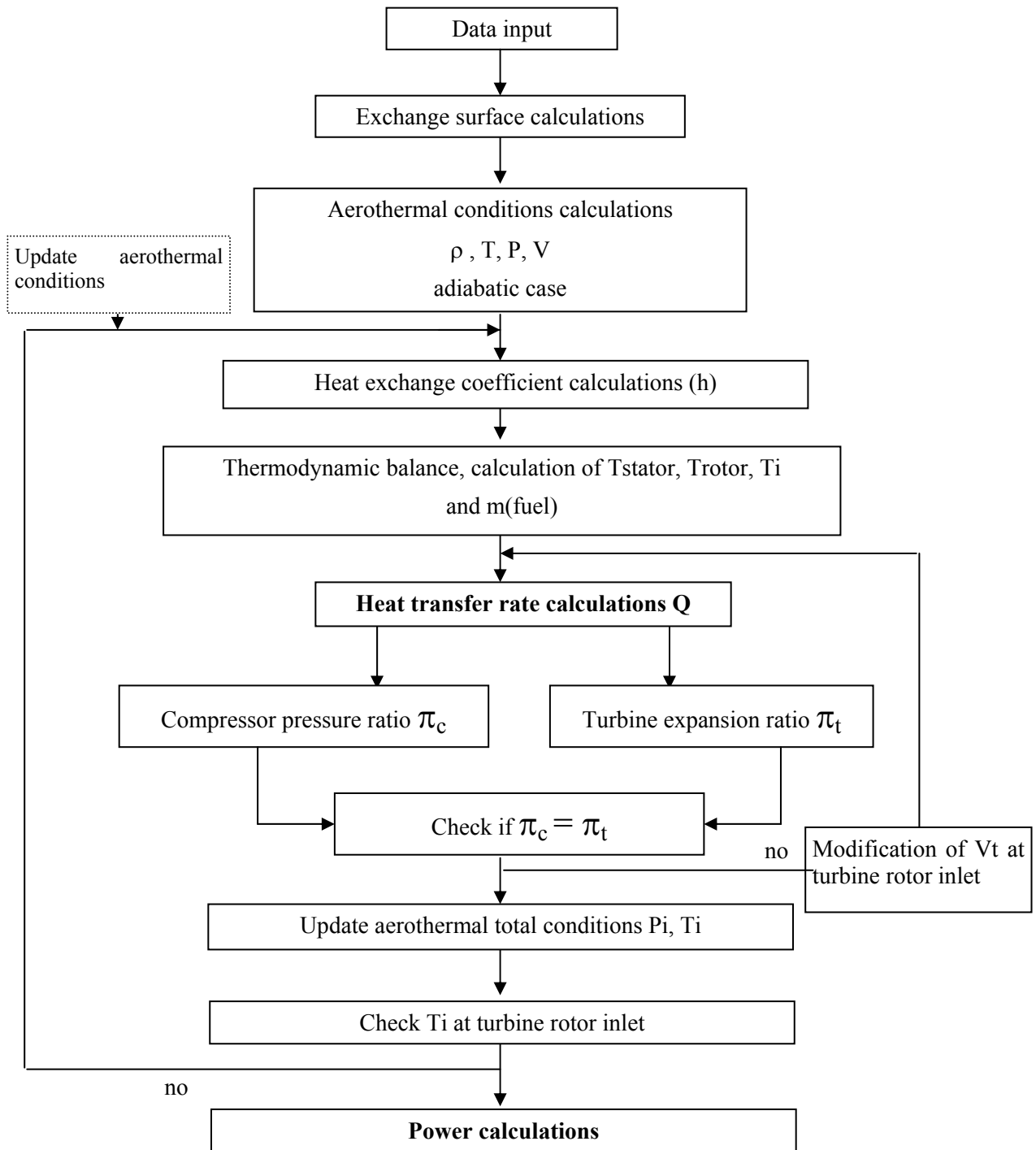


Figure 6: Non-Adiabatic Calculation Chart.

2.4 Results

The input values and an example of main calculation results for adiabatic operation are as follows (details are listed in Appendix 1):

Table 2: Input

Geometrical Data	Outer Radius of Rotor [m]	0.002
	Inner Radius of Rotor [m]	0.001
	Blade Height [m]	0.0004
	Outer Diameter of Casing [m]	0.012
Performance Data	Air Mass Flow Rate [kg / s]	0.0001
	Polytropic Compressor Efficiency (Adiabatic Flow)	0.7
	Polytropic Turbine Efficiency (Adiabatic Flow)	0.6
	Rotor Speed [rad / s]	2.5×10^5
	Combustion Efficiency (Adiabatic Flow)	0.95
	Combustor Temperature [K]	1600
	Initial Compression Ratio (Adiabatic Flow)	3.9
	Fuel Calorific Power (kerosene) [J / kg]	4.31×10^7
General Data	Fuel Heat Capacity [J / kg K]	1620
	SiC Thermal Conductivity [W / m K]	500
	SiC Emissivity	0.87

Table 3: Example of Results, Adiabatic Operation

Compressor Power [W]	21.49
Turbine Power [W]	35.81
Net Power [W]	14.32

2.4.1 Example of Results, Non-Adiabatic Operation

The following tables present the summary results obtained after convergence of all the calculations at non-adiabatic conditions for 1cm microturbine (detailed tables are listed in Appendix 2):

Table 4: Performance of Non-Adiabatic Micro Turbine

Stator Temperature [K]	990
Rotor Temperature [K]	769
Fuel Mass Flow Rate [kg/s]	2.76×10^{-6}
Specific Fuel Consumption [kg/J]	9.61×10^{-7}
Compressor Mechanical Power [W]	21.49
Turbine Mechanical Power [W]	24.36
Net Power [W]	2.87

2.4.2 First Conclusion

The comparison between the numeric results obtained for the adiabatic micro-turbine and for the non-adiabatic micro-turbine confirms the conclusions of the qualitative study of the aerothermodynamic problem.

- The compression ratio of the micro-turbine is not 3.9 (when adiabatic), but 3.4 approximately. The negative influence of the heat transfers on the compression ratio is thus well confirmed.
- The compression power remains the same but the expansion one decreases a lot; it reaches more than 35W for the adiabatic micro-turbine and is reduced to 25W approximately for the non-adiabatic one.
- The influence of the heat transfers is very negative here. There is on one hand a decrease of the compression ratio and thus the expansion rate, and on the other hand a cooling of the fluid in the turbine that still decreases the recoverable work.
- By accumulating the negative effects of the heat transfers in the compressor and in the turbine, the recoverable net power which reaches more than more than 14W for the adiabatic micro-turbine is reduced to 2.9W approximately for the non-adiabatic micro-turbine. With a so weak power, which does not even take into account the efficiency of the conversion of the transformation of mechanical energy into electrical energy in the starter-generator, the micro-turbine can't reach the performances which are foreseen for it.

2.5 Parametric Study of the Micro-Turbine Operation

This point presents short comments on the various existing possibilities to improve the performances of the micro-turbine concept. When it was possible, it also shows the calculations which were led by taking into account modifications brought to the initial micro-turbine concept.

2.5.1 Modification of Cycle Temperature

A modification of the high temperature of the cycle has consequences on the performances of the micro-turbine. So a decrease of this temperature should have two main consequences with opposite effects. On one hand, a decrease of the temperature of combustion decreases the temperature at turbine entrance.

The recoverable work on the turbine is then less important, as well as the net power of the micro-turbine. On the other hand, a decrease of the temperature of combustion should decrease the temperature of the micro-turbine stator and rotor parts. The heat exchanges between the fluid, the stator and the rotor should be thus minimised, with positive consequences on the net power of the micro-turbine. An increase of the temperature of combustion has inverse effects.

We will study the impacts on the micro-turbine net power with a decrease or an increase of the high temperature of the thermodynamic cycle.

Decrease of the High Temperature of the Cycle (TIT)

By keeping all the previous data and by following the same hypotheses, the calculations are run for the non-adiabatic micro-turbine with now a high temperature of the cycle taken successively at 1500K and 1400K.

The following tables present the summary calculation results (detailed table is listed in Appendix 3):

Table 5: Performance for $T_{comb} = 1500K$

Stator Temperature [K]	951
Rotor Temperature [K]	742
Fuel Mass Flow Rate [kg/s]	2.51×10^{-6}
Specific Fuel Consumption [kg/J]	1.43×10^{-6}
Compressor Mechanical Power [W]	21.49
Turbine Mechanical Power [W]	23.24
Net Power [W]	1.76

Table 6: Performance for $T_{comb} = 1400K$

Stator Temperature [K]	911
Rotor Temperature [K]	716
Fuel Mass Flow Rate [kg/s]	2.28×10^{-6}
Specific Fuel Consumption [kg/J]	4.18×10^{-6}
Compressor Mechanical Power [W]	21.49
Turbine Mechanical Power [W]	22.03
Net Power [W]	0.54

As visible on the tables the net power of the micro-turbine decreases, because it is 2.9W for a high temperature of 1600K, 1.8W for 1500K and 0.5W for 1400K. A decrease of the high temperature of the cycle thus has negative consequences on the performances of the micro-turbine. The heat exchanges decrease indeed, but not enough to overcome the loss of recoverable work on the turbine, which works at a lower temperature.

A decrease of the high temperature of the cycle is not thus a means to improve the performances of the MIT micro-turbine.

Increase of the High Temperature of the Cycle

This time the attempts are led with a high temperature of the cycle taken successively at 1700K, and at 1800K. The following tables give the summary results (detailed table is listed in Appendix 4):

Table 7: Performance for $T_{comb} = 1700K$

Stator Temperature [K]	1028
Rotor Temperature [K]	796
Fuel Mass Flow Rate [kg/s]	3.00×10^{-6}
Specific Fuel Consumption [kg/J]	7.52×10^{-7}
Compressor Mechanical Power [W]	21.49
Turbine Mechanical Power [W]	25.48
Net Power [W]	3.99

Table 8: Performance for $T_{comb} = 1800K$

Stator Temperature [K]	1065
Rotor Temperature [K]	823
Fuel Mass Flow Rate [kg/s]	3.25×10^{-6}
Specific Fuel Consumption [kg/J]	6.35×10^{-7}
Compressor Mechanical Power [W]	21.49
Turbine Mechanical Power [W]	26.61
Net Power [W]	5.12

The net power of the micro-turbine is more important when the high temperature of the cycle is increased. It could now develop a power of 5.1W for a temperature of 1800K.

An increase of the high temperature of the cycle thus seems to be a means to increase the performances of the micro-turbine. However, the gain in power is weak and is not enough to reach the 10 to 15 W which should supply the micro-turbine. On the other hand, a too important increase of the high temperature of the cycle is dangerous for the materials. We must remind that the melting point of the silicon carbide is close to 1800K.

2.5.2 Increase of the Size

The objective here is to decrease the heat transfers when compared to the net power developed by the micro-turbine by increasing the size of this last one. Indeed, this increase of size should decrease the influence of the scale factor and thus the impact of the heat transfers on the performances of the micro-turbine. This increase of size should naturally remain reasonable so that the micro-turbine remains a MEMS concept adapted to all the systems where it could be used.

So, a calculation was thus led with a micro-turbine with its dimensions multiplied by two. For this calculation, the size of the micro-turbine is 2.4cm in diameter and a 6mm in height.

This increase of the size is followed by several changes in the micro-turbine data. So, areas are multiplied by 4 and so is the air flow rate (it reaches here 0.4g/s); the volume is multiplied by 8 and so is the weight (it reaches here 8g). To keep a peripheral speed of 500m/s in rotor extremity, the rotation speed is divided by 2 to reach 125000rpm. On the other hand, the various blade and vane numbers remain the same in spite of the increase of the micro-turbine size.

Also, for simplification reasons, the compressor and turbine aerodynamic polytropic efficiencies were kept; in fact, considering the increase of the micro-turbine size, they should be a little bit better (Re effect).

Here are the calculations results (detailed table is listed in Appendix 5):

Table 9: Performance for Double-Sized Micro-Turbine

Stator Temperature [K]	972
Rotor Temperature [K]	777
Fuel Mass Flow Rate [kg/s]	1.18×10^{-5}
Specific Fuel Consumption [kg/J]	6.04×10^{-7}
Compressor Mechanical Power [W]	85.96
Turbine Mechanical Power [W]	105.43
Net Power [W]	19.48

The net power rises to 19.5W approximately for the non-adiabatic micro-turbine, against 53W for the adiabatic one in the same conditions.

The negative influence of the heat transfers is always present, but, as supposed, they have an impact less important on the micro-turbine performances. It underlines the importance of the scale factor in the MEMS study where strong heat transfers are present.

Whatever, the net power is important enough to allow the micro-turbine to be used on the applications demanding approximately 10 to 15W of power, as for portable energy sources or robot electric supply. The limited increase of the micro-turbine size thus seems to be a good solution to reach the performances foreseen for this concept.

However, this solution has a cost in weight. Besides the increase of the mass of the micro-turbine itself, there is an added weight of fuel; indeed, even if its specific consumption is better, the micro-turbine consumes more fuel when its size is doubled.

2.5.3 Disc Friction Losses

When doubling the size of the micro turbine, the disc friction power [5, 6] is only 18% of the net power instead of 66% for the original configuration.

If one can optimize the rotor/stator gaps of the main discs, the axial gap of the electric generator must be as small as possible in order to obtain a good electric efficiency. The Figure 7 gives the evolution of the net power as function of the axial electric generator gap. For the non insulated configuration the net power is very low for a gap less than 10 μ m. This means that the use of an electrostatic generator [7, 8] leads to a severe penalty in performances.

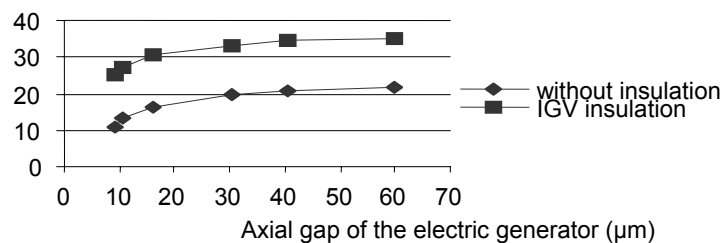


Figure 7: Net Power (Watts) versus Axial Gap.

2.5.4 Aerodynamic Efficiency

The product $\eta^2 = \eta_{pol\ comp} * \eta_{pol\ turb}$ of the aerodynamic polytropic efficiencies has a strong influence on the net power even in a non-adiabatic evolution. The Figure 8 shows the evolution of the net power versus this aerodynamic loss parameter, the reference non-dimensional power being obtained for $\eta^2 = 0.6 * 0.7 = 0.42$. For $\eta^2 = 0.31$ the micro turbine gives no more power.

Precise studies have been performed both on microcompressor [9] and microturbine [10] aerodynamics. The aerodynamic efficiency is mainly dependant on Reynolds number [11], specific speed [12], tip clearance ratio. At a first look it seems possible to obtain $\eta_{pol\ turb} > 0.6$ but it will be very difficult to obtain $\eta_{pol\ comp} > 0.7$.

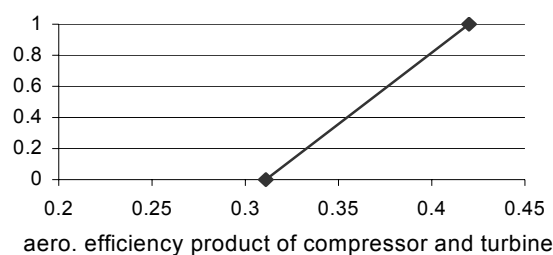


Figure 8: The Limit of Aerodynamic Efficiencies for Positive Net Power.

2.5.5 Heat Transfer Partial Insulation

In the hot button software one can insulate a component of the micro turbine by putting the corresponding heat transfer coefficients equal to zero. This methodology is interesting to understand the heat transfer organization and its influence on the performances. It is also useful to know which parts of the micro turbine must be insulated in priority in order to recover a part of the thermal efficiency. Some results of this parametric study are presented on Figure 9.

The calculations are performed in two situations. In the first one, $T_{\text{rotor comp}} = T_{\text{rotor turb}}$, configuration where the main disc is common to the compressor and the turbine or when the conduction in the shaft is dominant. In the second one, $T_{\text{rotor comp}} \neq T_{\text{rotor turb}}$, the heat transfer in the shaft is governed by its heat resistance.

The insulation of the burner alone is not very effective, this is because the heat transfer is transferred in the turbine and in a large part in the N.G.V. On the contrary the insulation of the N.G.V. appears to be much efficient. In this case the net power increases from 21.7 to 35 Watts ($T_{\text{rotor comp}} = T_{\text{rotor turb}}$) that is a 61% rise. The insulation of the compressor is also efficient but it seems practically difficult to manage it both on the rotor and on the stator.

When the heat transfer between the turbine rotor and the compressor rotor is driven by the thermal resistance of the shaft, a moderate gain in net power is obtained. But this apparent gain is cancelled by the additional disc friction losses occurring when three discs operate instead of two (two for the compressor rotor and one for the turbine rotor).

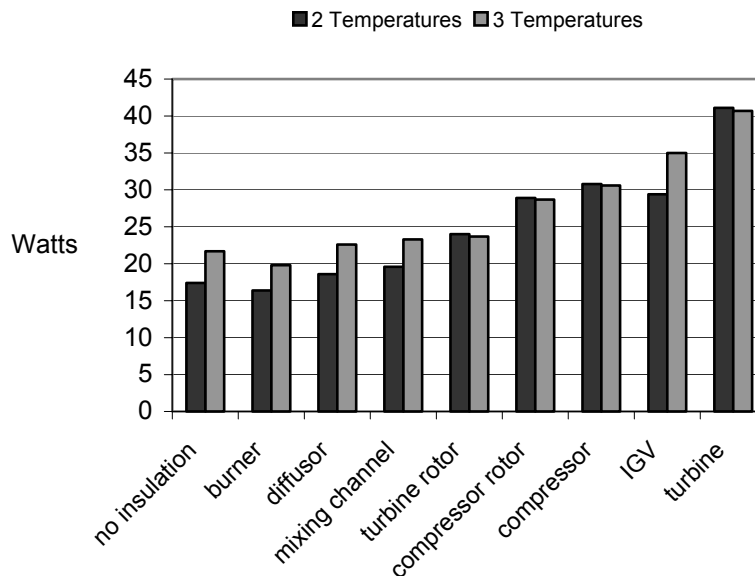


Figure 9: Net Power for Partial Thermal Insulation.

2.5.6 External Heat Losses

In order to try to enhance the performances of the micro turbine, the benefit effect of a heat shield with a thickness of 2mm was studied. A simple calculation was performed assuming that, as the first approximation, the temperature of the stator is not changed. This is not really true because some insulation rises the temperature of the stator but this gives a good order of the magnitude of the temperature

difference between the stator (SiC or Si) and the outside skin. This simple model, independent of the “hot button software”, satisfies steady heat flux conditions at the boundaries of the coating, with a plane or a spherical conduction scheme.

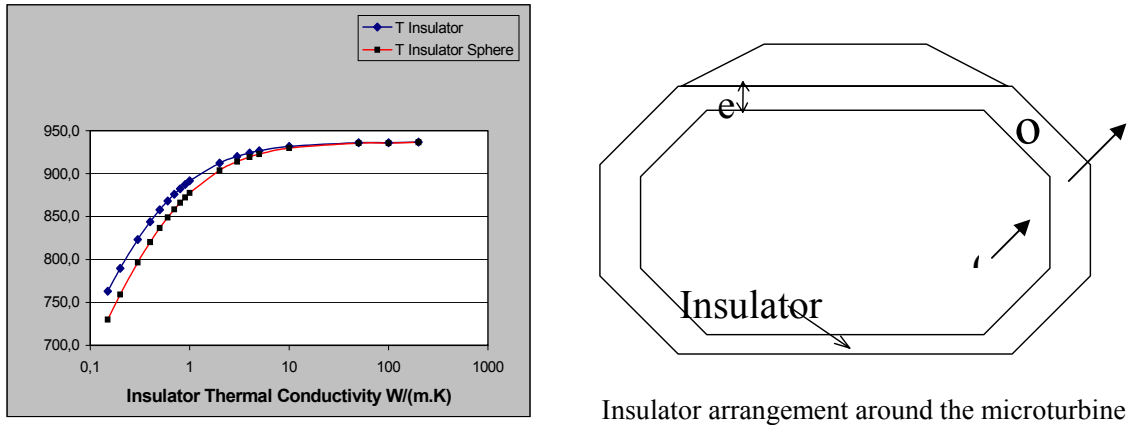


Figure 10: Insulator Temperature Function of the Thermal Conductivity
(μ turbine $\phi = 1$ cm, emissivity = 0.87).

For a 2mm insulator, the material is efficient if its thermal conductivity is less than 1 (Figure 10). In particular the conductivity of SiO₂ which is about 2 at high temperature seems too important except if we decrease the emissivity by an appropriate surface deposit.

A second method to know the evolution of the performances of the micro turbine, is to use “the hot button” software by studying the influence of the emissivity parameter of the outside skin (Figure 11). Even if the results show some oscillations in convergence, we can estimate that the maximum gain in net power is about ten percent.

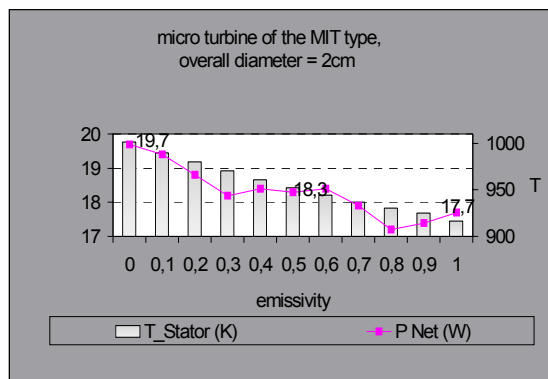


Figure 11: Emissivity Influence on the Performances.

Remark:

The “hot button” software is built to handle different types of fuels: H₂, kerosene, methane and propane. Precise thermodynamic laws depending on the gas composition and the temperature are introduced. The simple convective heat transfer coefficient operating in the NGV is validated with two different ways, first a boundary layer calculation of the integral method type (thanks to M. Cousteix from ONERA) was developed, then the heat transfer in the NGV was also determined by applying a NS 3D solver (Elsa NS 3D ONERA code) to the microturbine stage. Both methods gave results similar with the more simple formulation introduced in “hot button” [10, 14].

2.6 Summary

An aerothermodynamic model on Power-MEMS type micro-gas turbine energetic behavior, which takes into account strong heat transfer, was developed and applied in different situations. The applications of the corresponding software “hot button” points out important results as follow:

- First at the MIT original scale (one centimetre diameter), the isothermal constraint on the material gives rise to strong heat transfer which alter badly the net power of the engine, and the increase in TIT has a weak influence on the performances.
- The most simple solution found to recover a useful power of the order of 15W is to multiply the dimensions by a factor of two. It is interesting to note that the new MIT micro-turbine prototype has a size doubled from the initial concept.
- The heat insulation of N.G.V. allows to recover a large part of the lost power, but the question is: is it possible to realize this insulation by micro-technology technique?
- The insulation of combustion chamber alone does not work. This means that the good efficiency to maintain in this component is the chemical efficiency. The present results suppose that the chemical efficiency is nearly one, so that there is good mixing between air and fuel, good mixing between hot burnt gases and fresh carburated air, sufficient volume in the combustion chamber so that all the fuel is burnt.
- The dramatic influence of compressor and turbine efficiency is confirmed in a non-adiabatic operation.
- The use of a low conductivity material for the stator would improve by a large amount the performances.
- The external radiative heat losses are estimated to ten percent of the nominal power for the 2cm diameter microturbine. A thermal shield of 2mm thickness is a good way to enhance the performances and is certainly a necessity for integration.
- A better knowledge of the heat transfer coefficients at low Reynolds numbers in the different components of the micro turbine has to be obtained to refine the results of this study.

Finally, at this step of research, it is yet to be concluded on the viability of the MEMS microturbine concept (microturbine on a SiC chip) on an energetic point of view. More information is still needed on the aerodynamic efficiency level of the turbomachines, which depends for a large part of the relative tip clearance of the rotors and of the depth SiC etching capability (specific speed dependence).

Knowledge is also necessary for the energetic consumption of gas bearings (journal and thrust gas bearings) [13] and also of the magnetic type electric motor.

Finally, the insulation capability is needed for some parts of microturbine by microtechnology technique.

The present model, when well documented with complementary information and refinements on heat transfer coefficients, turbomachinery aerodynamic efficiency function of tip clearance, Re number, specific speed, seems a proper tool to guide in the good direction the design, from an energetic point of view.

3 WAVE ROTOR INTEGRATION

As shown in the previous section, the performance of ultra-micro gas turbine will not be so good as that of conventional size, although its power and energy densities are still larger than batteries. In general, topping cycle is one of the effective methods to improve the gas turbine performance. A promising candidate for performance improvement is a heat exchanger, which is already used in micro gas turbine

system, whereas it may lead large total pressure loss and weight increase in the ultra-micro gas turbine. Also, a heat exchanger may not be a good solution, when this ultra-micro gas turbine is used as the propulsion system of micro air vehicles.

Therefore, a possibility of wave rotor topping cycle is described in this section. Wave rotors are expected to have a potential to improve drastically the performance of a gas turbine system [15-17]. A wave rotor consists of a rotor and ports as shown in Figure 12, and the rotor consists of many narrow channels called “cells”, in which the working gas compression / expansion takes place. Each port, which is connected to the gas turbine component, charges or discharges the cells with fresh air or combustion gas, respectively.

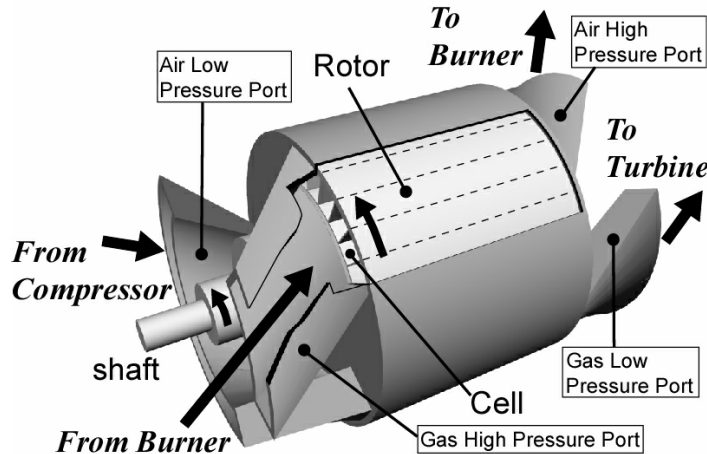


Figure 12: Wave Rotor.

A wave rotor can be topped on a gas turbine as shown in Figure 13, so that it plays a role of pressure and heat exchangers. Therefore, the maximum temperature and total compression ratio can be raised without much difficulty in the other gas turbine components, yielding pressure gain at the turbine inlet, as shown in the T-S diagram. In addition, larger benefit will be achieved by topping a wave rotor, when the baseline gas turbine is small and its total compression ratio is low, according to the cycle analysis of whole system [19], although such small ones as ultra-micro gas turbines (Figure 1) have never been discussed.

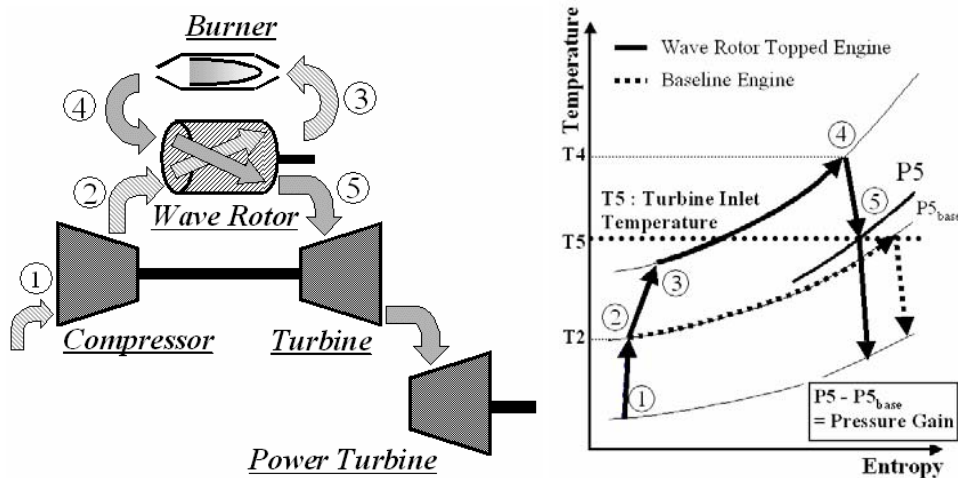


Figure 13: Wave Rotor Topping Cycle.

3.1 Working Principle

Figure 14 is the “wave diagram” which shows the pressure wave dynamics schematically with characteristic lines. This figure shows the diagram of 4-port through flow wave rotor [17], which is supposed to be appropriate for a gas turbine cycle. In this figure, an example of the total pressure and temperature in each port, which are normalized by the condition in Air-LP (Air Low Pressure Port), are indicated just for reference. Here, the upper half of this diagram is called “compression process”, and the bottom half is called “expansion process” respectively.

At the beginning of the cycle (at the top of the rotor in this figure), the left half of the cell is filled with low pressure air from Air-LP, while the right half is filled with low pressure combustion gas brought over from the previous rotation. At this moment, the air and gas are almost stationary.

3.1.1 Compression Process

When the cell is exposed to Gas-HP (Gas High Pressure Port), the combustion gas of high pressure and temperature from the burner rushes into the cell, and “primary shock wave” is generated by the pressure difference. This shock wave propagates to the right, and reflects at the end of the cell. This reflected shock wave is called “secondary shock wave”, and propagates back to the left side. The gas and air in the cell is compressed by these two shock waves, and flows out to the Air-HP (Air High Pressure Port), which is opened to the cell just after the shock wave reflection. When the secondary shock wave reaches to the left end of the cell, Gas-HP is closed and a rarefaction wave is generated by the inertia of inflow gas. When this rarefaction wave reaches to the right end of the cell, Air-HP is closed. Consequently, the air and gas in the cell is compressed and flows out to the combustion chamber through Air-HP, and the cell is filled with high pressure combustion gas.

3.1.2 Expansion Process

When the cell is exposed to Gas-LP (Gas Low Pressure Port), the high pressure gas in the cell flows out to this port, and an expansion wave (fan) is generated and propagates to the left. When this expansion fan reaches to the left end and the pressure in the cell becomes low enough, Air-LP (Air Low Pressure Port) is opened to the cell and fresh air flows into the cell. Gas-LP is closed with generating a compression wave by the sudden stop of outflow, and the air is charged in the left half of the cell. Air-LP is closed when this compression wave reaches to the left end. By this process, the condition in the cell becomes the same as that at the beginning of the cycle.

As seen in this process, a wave rotor has an advantage for the heat resistance, because hot gas and cold air flow through the cells alternately, which also yields heat regenerative effect in the Brayton cycle. This means that the temperature of combustion chamber can be raised without particular concern about the cooling technology of turbine blades, even though the limitation is still remained because of the cooling of ports and chemical process of combustion itself.

A point of wave rotor design is to precisely predict the propagating velocity of pressure waves, because each port should be opened and closed to the cells in accordance with the arrival timings of pressure waves at the end of the cells, as shown in Figure 14. But its prediction is not so easy, because the propagating velocity of pressure waves is much affected by the inherent features of wave rotors, which will be described later in this section.

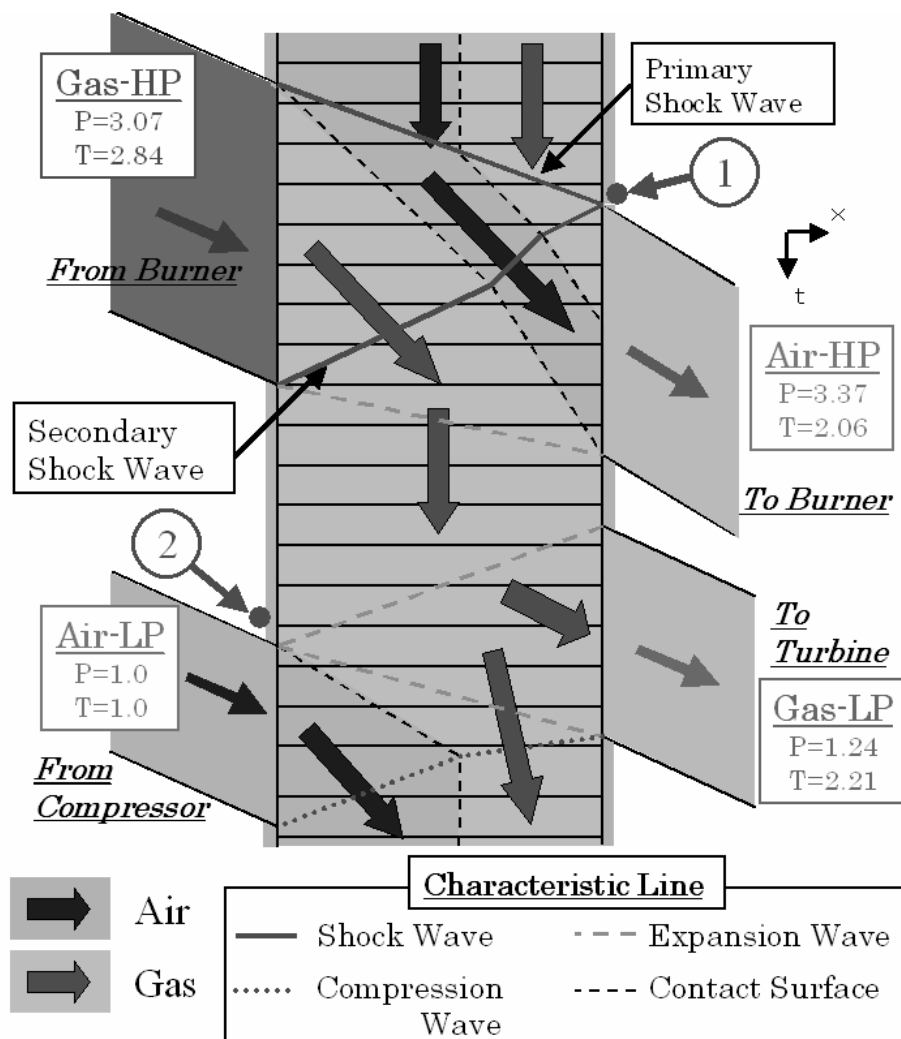


Figure 14: Wave Diagram.

3.2 Impact of Wave Rotor Topping

To estimate the performance improvement, the results of cycle analysis are described in this section.

3.2.1 Numerical Model

The whole system was considered to be comprised of the baseline gas turbine and a wave rotor topping. In the present cycle analysis, heat transfer effect was taken into account as shown in Figure 15, in reference to the treatment of Hot Button Software described previously.

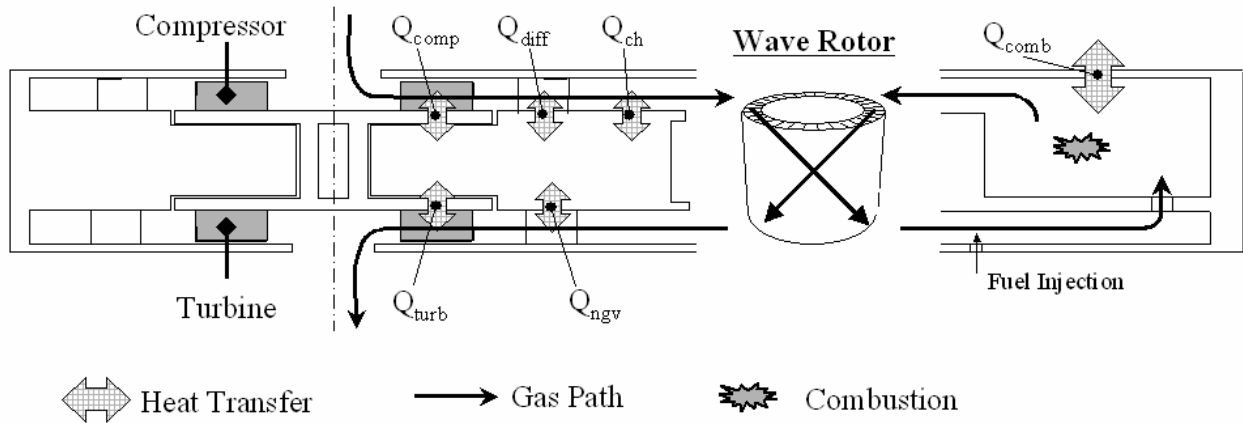


Figure 15: Scheme of Cycle Analysis in Wave Rotor Topped Ultra-Micro Gas Turbine.

3.2.1.1 Compressor Rotor

The basic equations are in accordance with the “hot button software”, so that the heat transfer value “ Q_{comp} ” is decided explicitly by the result of “hot button”. Here, λ is the ratio of the heat transfer and mechanical work defined as

$$\lambda_{comp} \equiv -\frac{Q_{comp}}{W_{comp}} \quad (\text{notice: Heat transfer from fluid to solid wall is positive here.})$$

Then, the necessary mechanical work for compressor rotor can be described as,

$$W_{comp} = \left[\frac{\dot{m}_{air} \cdot C_{p_{air}} \cdot T_{in}}{1 + \lambda_{comp}} \right] \cdot \left[\left(\frac{P_{out}}{P_{in}} \right)^{\frac{R_{air} \cdot (1 + \lambda_{comp})}{C_{p_{air}} \cdot \eta_{comp}}} - 1 \right]$$

where the efficiency of compressor η_{comp} is polytropic efficiency, which is fixed.

The value of λ_{comp} is calculated by the iterative calculation of these two equations, given the compression ratio P_{out} / P_{in} .

With calculated λ_{comp} , the temperature at compressor rotor exit can be calculated as below.

$$T_{out} = T_{in} \cdot \left(\frac{P_{out}}{P_{in}} \right)^{\frac{R_{air} \cdot (1 + \lambda_{comp})}{C_{p_{air}} \cdot \eta_{comp}}}$$

3.2.1.2 Diffuser

In diffuser, the air is assumed to be heated by the stator wall with constant pressure, therefore the condition change can be described as below.

$$P_{out} = P_{in}$$

$$T_{out} = T_{in} - \frac{Q_{diff}}{\dot{m}_{air} \cdot Cp_{air}}$$

3.2.1.3 Mixing Channel

Also in mixing channel, the fluid is heated at constant pressure, with fuel added at the inlet.

$$P_{out} = P_{in}$$

$$T_{out} = \frac{\dot{m}_{air} \cdot Cp_{air} \cdot T_{in} + \dot{m}_{fuel} \cdot Cp_{fuel} \cdot T_{atm} - Q_{ch}}{\dot{m}_{air} \cdot Cp_{air} + \dot{m}_{fuel} \cdot Cp_{fuel}}$$

Here, the mass flow rate of fuel is not known to be calculated by the iterative calculation of “mixing channel” and “combustor” components. However, this iteration is not necessary for the wave rotor topped gas turbine analysis, because fuel is not added in the mixing channel in this case.

3.2.1.4 Combustor

Here, the combustion temperature (T_{comb}), combustion efficiency (η_{comb}), heat transfer (Q_{comb}), and Lower Heating Value of fuel (LHV) are fixed, and the mass flow rate of fuel (m_{fuel}) can be calculated as written below.

$$\dot{m}_{fuel} = \frac{Cp_{gas} \cdot T_{comb} - Cp_{air} \cdot T_{in}}{\eta_{comb} \cdot LHV - Cp_{gas} \cdot T_{comb} + Cp_{fuel} \cdot T_{in}} \cdot \dot{m}_{air}$$

After combustion, the fluid temperature is decreased by heat transfer, and the exit temperature can be described as follows.

$$T_{out} = T_{comb} - \frac{Q_{comb}}{(\dot{m}_{air} + \dot{m}_{fuel}) \cdot Cp_{gas}}$$

3.2.1.5 Nozzle Guide Vane

In nozzle guide vane, the fluid temperature is decreased by heat transfer at constant pressure. Therefore the outlet condition can be calculated as follows.

$$P_{out} = P_{in}$$

$$T_{out} = T_{comb} - \frac{Q_{comb}}{(\dot{m}_{air} + \dot{m}_{fuel}) \cdot Cp_{gas}}$$

3.2.1.6 Turbine Rotor

As in the compressor rotor calculation, the equations for turbine rotor can be described as follows with polytropic efficiency η_{turb} .

$$\lambda_{turb} \equiv -\frac{Q_{turb}}{W_{turb}}$$

$$W_{turb} = \frac{(\dot{m}_{air} + \dot{m}_{fuel}) \cdot Cp_{gas} \cdot T_{in}}{1 - \lambda_{turb}} \cdot \left[1 - \left(\frac{P_{out}}{P_{in}} \right)^{\frac{R_{gas} \cdot \eta_{turb} \cdot (1 - \lambda_{turb})}{Cp_{gas}}} \right]$$

$$T_{out} = T_{in} \cdot \left(\frac{P_{out}}{P_{in}} \right)^{\frac{R_{gas} \cdot \eta_{turb} \cdot (1 - \lambda_{turb})}{Cp_{gas}}}$$

Here, P_{out} is set to be atmospheric.

3.2.1.7 Wave Rotor

A simple thermodynamic approach to the wave rotor characteristics can be found in the previous work of NASA G.R.C. [16]. In this approach, energy exchange between combustion gas and air was treated as compression and expansion works of the fluids (W_{WRCP} , W_{WREP}), assuming the adiabatic compression and expansion efficiencies of η_{WRCP} and η_{WREP} . Here, the subscriptions of *GHP*, *GLP*, *AHP*, and *ALP* indicate the Gas-HP, Gas-LP, Air-HP, and Air-LP, respectively.

$$W_{WRCP} = \dot{m}_{air} \cdot Cp_{air} \cdot (T_{AHP} - T_{ALP}) = \frac{\dot{m}_{air} \cdot Cp_{air} \cdot T_{ALP}}{\eta_{WRCP}} \cdot \left[\left(\frac{P_{AHP}}{P_{ALP}} \right)^{\frac{R_{air}}{Cp_{air}}} - 1 \right] \quad (24)$$

$$W_{WREP} = (\dot{m}_{air} + \dot{m}_{fuel}) \cdot Cp_{gas} \cdot (T_{GHP} - T_{GLP})$$

$$= (\dot{m}_{air} + \dot{m}_{fuel}) \cdot \eta_{WREP} \cdot Cp_{gas} \cdot T_{GHP} \cdot \left[1 - \left(\frac{P_{GLP}}{P_{GHP}} \right)^{\frac{R_{gas}}{Cp_{gas}}} \right] \quad (25)$$

Here, the compression ratio (P_{AHP} / P_{ALP}) is fixed. Therefore, T_{AHP} can be calculated with the equation (24). Moreover, P_{GLP} can be described with introducing $W_{WRCP} = W_{WREP}$ as below.

$$P_{GLP} = P_{GHP} \cdot \left\{ 1 - \frac{\dot{m}_{air}}{\dot{m}_{air} + \dot{m}_{fuel}} \cdot \frac{1}{\eta_{WRCP} \cdot \eta_{WREP}} \cdot \frac{Cp_{air}}{Cp_{gas}} \cdot \frac{T_{ALP}}{T_{GHP}} \cdot \left[\left(\frac{P_{AHP}}{P_{ALP}} \right)^{\frac{R_{air}}{Cp_{air}}} - 1 \right] \right\}^{\frac{Cp_{gas}}{R_{gas}}}$$

And now T_{GLP} can be calculated by the equation (25) with obtained P_{GLP} .

3.2.2 Results

3.2.2.1 Double Sized Gas Turbine of MIT Type

Table 10 shows the common input values for the present analysis. Here, kerosene is used as fuel, and physical values (Cp , R , etc.) are fixed during calculation. Table 11 shows the input values for double

sized Power-MEMS turbine of MIT type. Also, Table 12 shows the heat transfer value in each component, which was obtained by Hot Button Software with the same input condition. For reference, the performance of baseline engine calculated by the present numerical model is shown in Table 13.

Table 10: Common Input Parameter

Cp of air [J/kg K]	1040
Gas Constant of air [J/kg k]	287.4
Cp of combustion gas [J/kg K]	1250
Gas Constant of combustion gas [J/kg K]	287.8
Cp of fuel [J/kg K]	1620
Ambient Pressure [Pa]	101325
Ambient Temperature [Pa]	288
Lower Heating Value of fuel [J/kg]	43100000

Table 11: Input Parameter for Double Sized Ultra-Micro Gas Turbine of MIT Type

Compression Ratio of Compressor	3.27
Mass Flow Rate of Air [kg/s]	0.0004
Temperature in Combustor [K]	1600
Compressor Efficiency (Polytropic)	0.7
Turbine Efficiency (Polytropic)	0.6
Combustion Efficiency	0.95

Table 12: Heat Transfer

Component	Heat Transfer [W]
Compressor Rotor	-34.16
Diffuser	-42.26
Mixing Channel	-51.22
Combustor	34.57
Nozzle Guide Vane	120.75
Turbine Rotor	30.18

Table 13: Performance of Baseline Engine

Net Power [W]	18.8
Fuel Mass Flow Rate [kg/s]	1.2×10^{-5}
Thermal Efficiency [%]	3.6
SFC	6.38×10^{-7}

In this analysis, the temperature in combustor was fixed, which yields lower turbine inlet temperature in the wave rotor topped cycle. Therefore, the heat transfer values in nozzle guide vane and turbine rotor were estimated by assuming that they are proportional to the temperature difference between the wall and fluid temperature at the inlet of each component. Here, the temperatures of wall and turbine rotor were set as 930K and 848K respectively, which were obtained by the Hot Button Software. The heat transfer in the wave rotor component was not considered, therefore its effect was included in the compression and expansion efficiency. Here, those efficiencies of wave rotor were set as 0.83, in reference to the previous work on the wave rotor [16, 19].

Figure 16 shows the plot of performance ratio (Wave Rotor Topped Performance / Baseline Performance) with changing the wave rotor compression ratio from 1 to 3. As seen in this plot, the gains of net power, thermal efficiency and sfc (specific fuel consumption) are about 20%, and its peak is achieved at about 1.6 of the wave rotor compression ratio.

This result seems not so attractive with complicated system and control of wave rotor topping cycle. However, if the heat transfer in mixing channel is assumed to be adiabatic, the plot is changed drastically as shown in Figure 17. The improvement of thermal efficiency reaches more than 40% of baseline engine, and the peak is achieved at about 2 – 2.6 compression ratio, which seems to be adequate for the wave rotor operation. Therefore, it is very important to reduce the heat transfer in mixing channel, when a wave rotor is applied to an ultra-micro gas turbine.

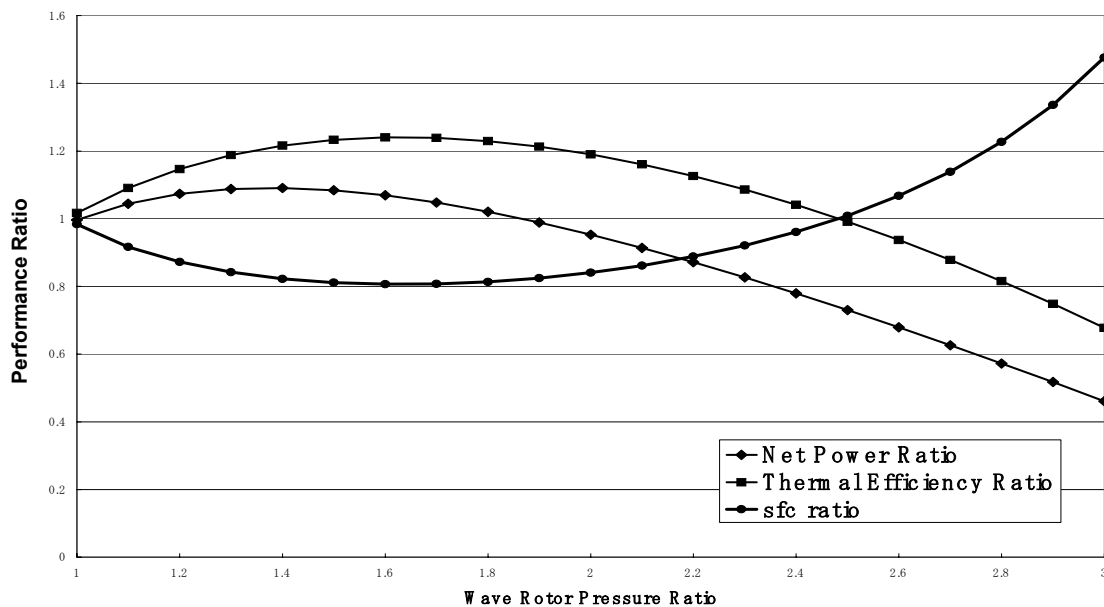


Figure 16: Performance Gain of Wave Rotor Topping Cycle (Double Size of MIT Type).

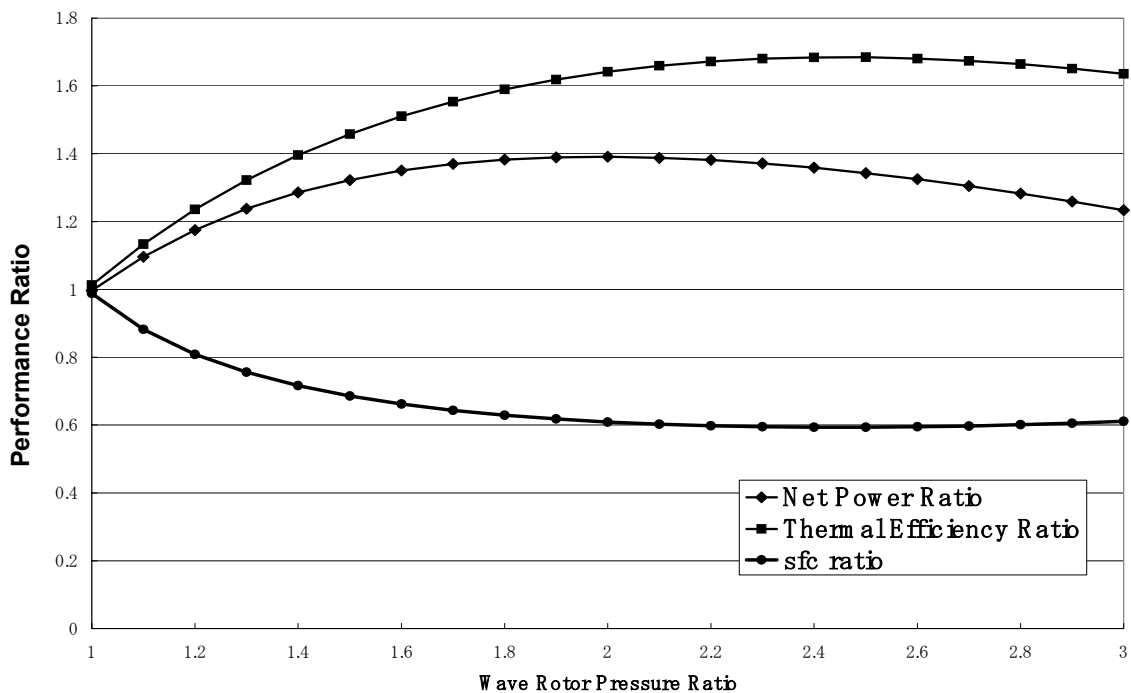


Figure 17: Performance Gain without Heat Transfer in the Mixing Channel.

3.2.2.2 Wave Rotor Topping on the Micro Gas Turbine of NEDO Project

Another ultra-micro gas turbine, Palm-top, has been designed with a list of specification in Table 14. The size of Palm-top gas turbine is almost 10 times larger than the MIT Power-MEMS turbine. Therefore, the effect of heat transfer is not so serious in this case, so that each component was assumed to operate adiabatically. In this design, the maximum temperature was set in accordance with the heat resistance of turbine rotor material. Therefore, the temperature in the combustor can be raised, with TIT given the same for the wave rotor topped cycle, so that the temperature in the combustor was set as 1360K here.

Table 14: Input Parameter for Palm-top Gas Turbine

Compression Ratio of Compressor	2.5
Mass Flow Rate of Air [kg/s]	0.03
Turbine Inlet Temperature [K]	1223
Compressor Efficiency (Polytropic)	0.7
Turbine Efficiency (Polytropic)	0.6
Combustion Efficiency	0.99

Figure 18 shows the result of this case. The performance gain is getting better at the higher wave rotor compression ratio, although its value of 4.0 seems a little too high in practice. Also, the performance of wave rotor topped cycle reaches more than 2.5 times better than the baseline engine, which is far better than that due to MIT Power-MEMS turbine.

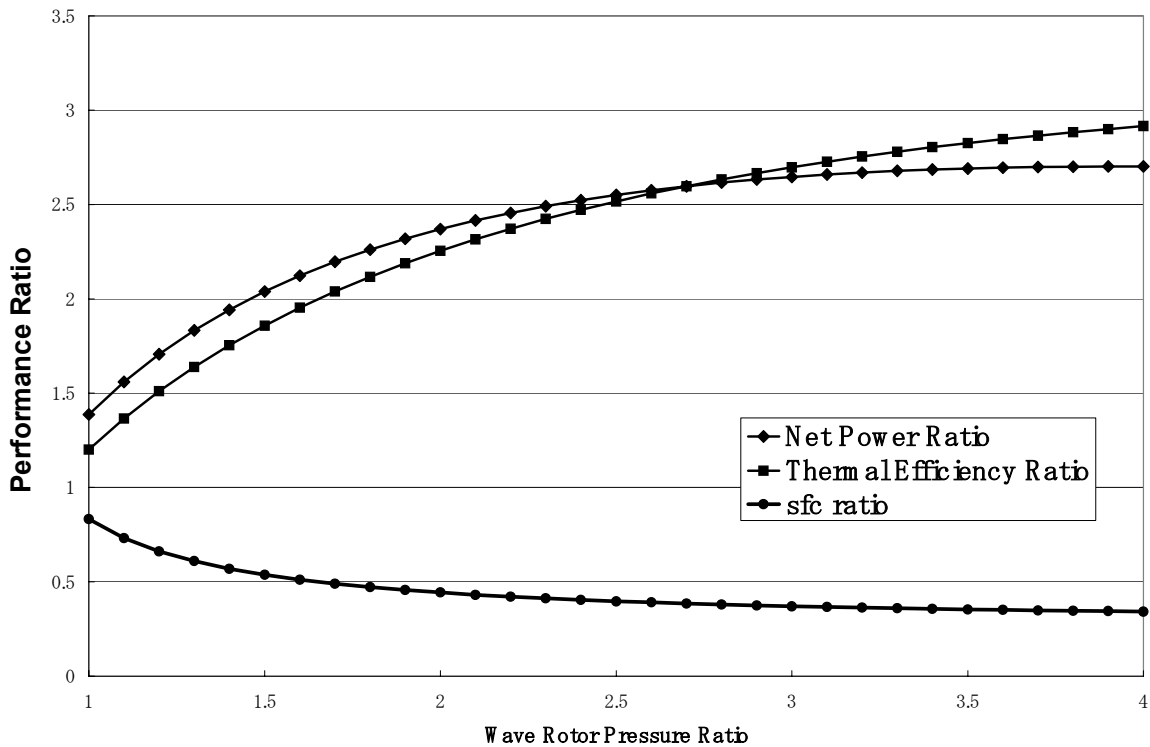


Figure 18: Performance Gain of Wave Rotor Topping Cycle (Palm-Top Gas Turbine).

3.3 Investigation of Inner Flow Dynamics

According to the experimental works performed by NASA G.R.C. [21, 22], three dominant factors were identified in the estimation of performance loss mechanisms, that is, “Gradual Passage Opening,” “Viscosity,” and “Leakage.” As described in section 3.1 “Working Principle,” the most important point in the wave rotor design procedure is the prediction of propagating velocity of pressure waves. Therefore, it is significant to understand how these factors affect the inner flow dynamics, especially, the wave propagation. In this section, both 2D numerical simulation and experimental visualization are described, and the effect of each factor on the inner flow dynamics is discussed.

3.3.1 Experimental Visualization

In the long history of wave rotor research, many experiments have been carried out, although any attempts are not found to look inside of the cells, except for perhaps the only one work for an internal combustion wave rotor [24]. Therefore in this study, test equipment adopting a new concept was devised in the experiment to visualize the inner flow dynamics of a wave rotor (Figure 19) [25, 26]. In this design concept, the cell is fixed stationary, whilst the ports are rotating, so that the reflecting schlieren method and direct measurement of wall static pressure can be employed directly to the stationary cells. A care is therefore needed that the “rotors” in Figure 19 mean the rotating ports to charge / discharge the working gas. These rotors are connected to a bevel gear, and driven by an electric motor. Here, Gas-HP settled side is called “Gas Side”, and the Air-HP settled side is called “Air Side”. In the experiment, compressed air at the room temperature is used as the combustion gas, and the pressure ratio between the gas and air is 2.6. The rotational speed is 4200rpm, and the mean rotor radius is 60mm. The cell length is 186mm, the width is 8mm, and the height is 16mm. Three cells are installed in the test section, because the effect of leak flow in the circumferential direction will appear from the interaction between the neighboring cells, while the effect of leak flow in the radial direction can be treated as the leak flow to the surroundings. The principal object for the measurements is the cell at the centre.

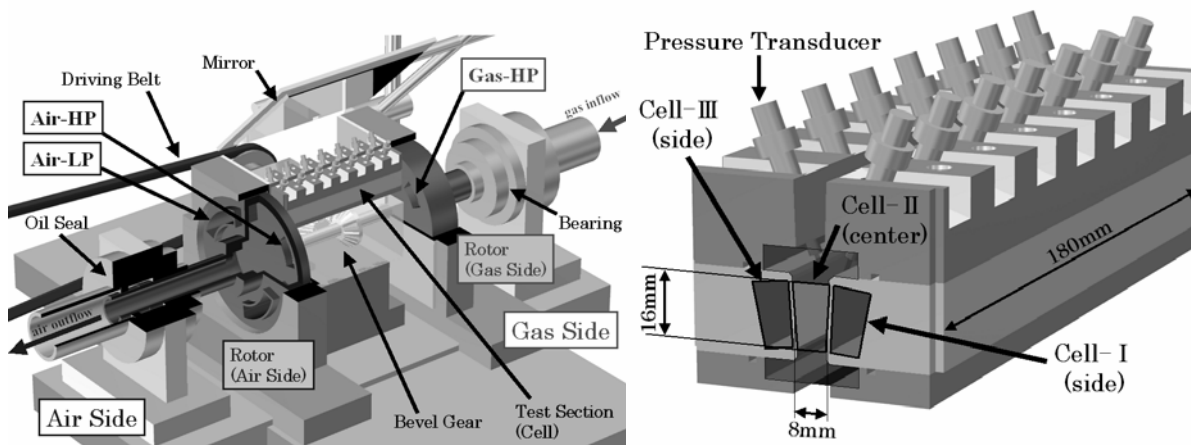


Figure 19: Experimental Apparatus for Visualization [26].

Figure 20 shows the schlieren pictures of the primary and secondary shock waves observed in this experiment. The “DT” at the left end of this figure indicates the time elapsed from the moment when Gas-HP starts opening upwards from the bottom at the cell end. The primary shock wave propagates to the right, but was not observed before $DT=200\mu s$, because the intensity of the primary shock was too weak at the beginning of the cycle. On the other hand, the secondary shock wave is always a normal shock wave, which propagates to the left. Furthermore, extra pressure waves appear in the pictures (lines 2&4 index). These pressure waves are considered to be generated by the reflection of the primary shock waves at the neighboring cells, judging from its originating instances.

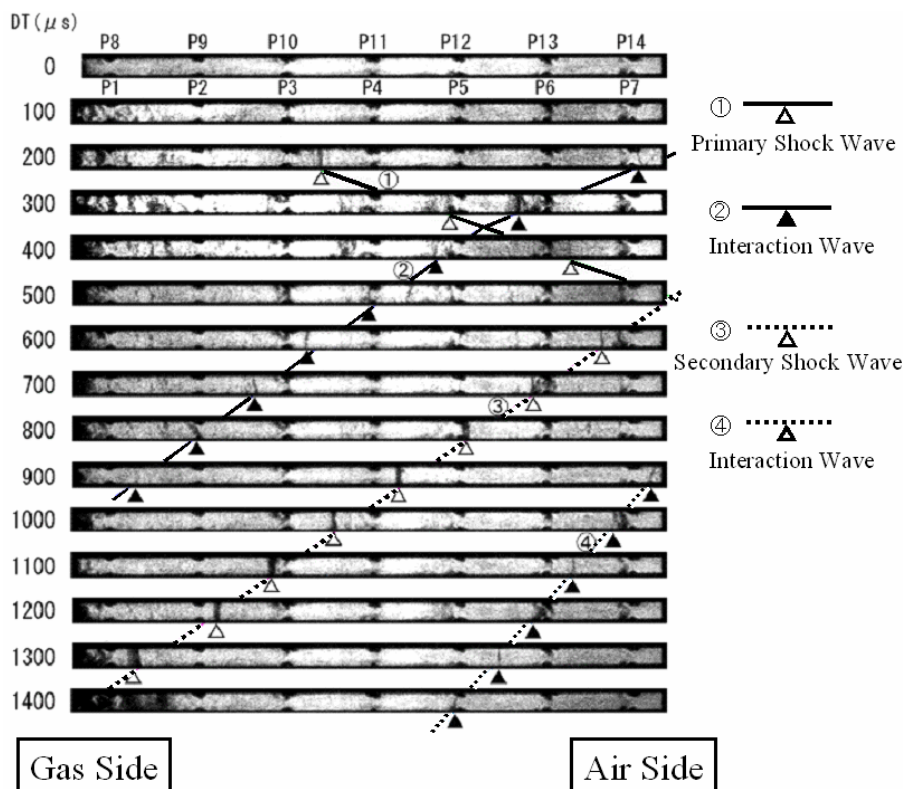


Figure 20: Schlieren Pictures [26].

3.3.2 2D Numerical Simulation

In the previous wave rotor research, both 2D and 3D numerical simulations were carried out [27-30]. In the present study, 2D numerical simulation at the mean radius plane was attempted to investigate the influence of gradual passage opening and leakage effects on the inner flow dynamics [25, 26]. The governing equations are 2D Reynolds averaged Navier-Stokes equations with laminar viscosity. The solution scheme is based upon Finite Difference Method discretization, incorporating Chakravathy-Osher's 3rd order upwind TVD scheme with the van Leer's differentiable limiter. As for the time integration, the Jameson-Baker's four-stage Runge-Kutta scheme (fourth-order accuracy) was adopted.

The cell size, the ports' conditions, and any other conditions are set to the same as those of the experiment. The mesh is 601 x 31 in each cell. The inflow and outflow conditions are decided by solving one-dimensional (axial direction) Riemann problem locally with the application of Riemann invariance [31]. In this simulation, leak flow effect in the radial direction, as well as that in the circumferential direction, is taken into account by estimating the flux across the surrounding conditions with the application of Riemann invariance.

Figure 21 shows a time series of the non-dimensional density contour wherein three cells are solved simultaneously just as in the experiments. The state in each port is assumed to be uniform during the calculation, and the ports are gradually opening to the cells from bottom to top.

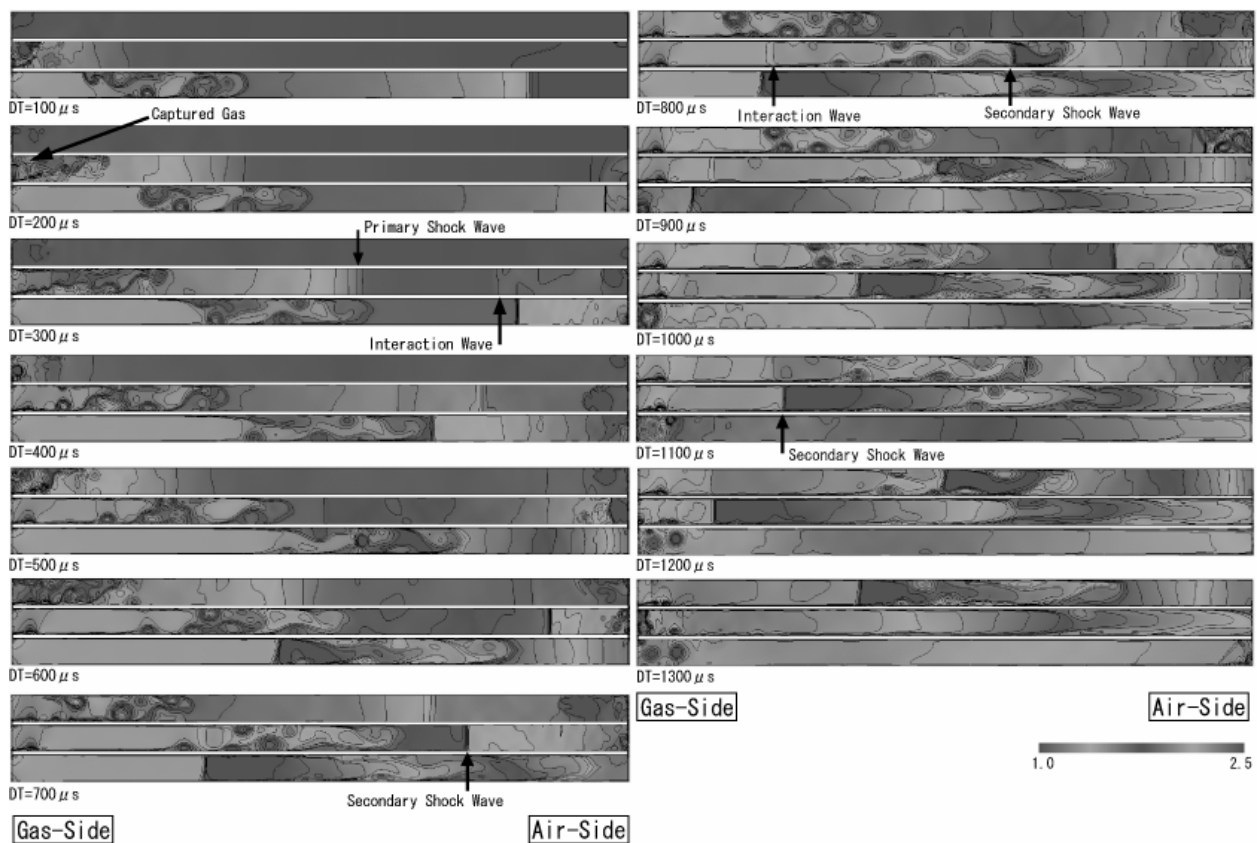


Figure 21: Numerical Result of Multi Passage Simulation (Density Contour) [26].

The primary and secondary shock waves are seen to be in good agreement with the schlieren pictures, which has also been confirmed quantitatively by the time traces of wall static pressure measurements [26]. The interaction wave between the neighbouring cells also appears in the numerical results. Figure 22

shows the enlarged illustration at the instance of the interaction wave generation. In this figure, the pressure rises at the cell end of the air side due to the reflection of the shock wave, which yields the flow in the circumferential direction through the clearance region, and finally the interaction wave is generated.

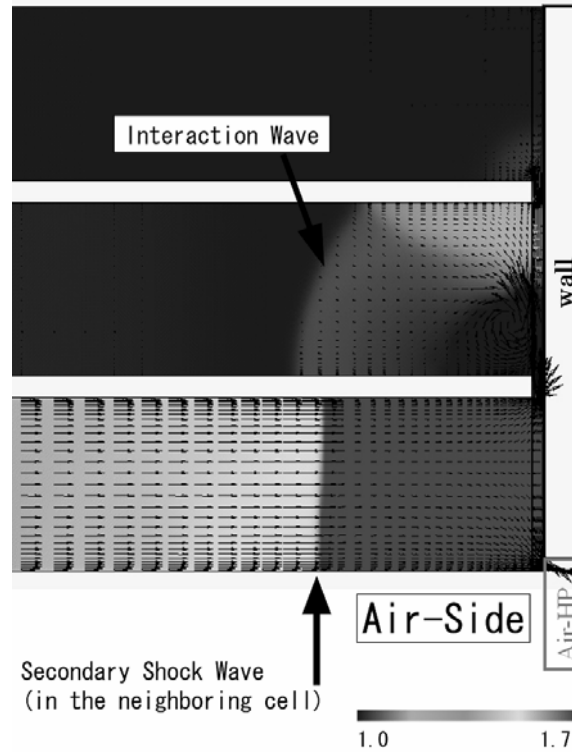


Figure 22: Interaction Wave [26].

3.4 Overall Simulation Model

3.4.1 Numerical Modelling

As described above, it is necessary for the wave rotor design to accurately simulate the pressure waves generated in the cells. It has been confirmed that 2D numerical code can simulate the pressure waves precisely, but its calculation cost is too expensive to be used in designing the wave rotors. Therefore, more practical over-all simulation model has been developed to assist its design [32, 33]. The similar approach can be found in several works [34-38], though the modelling is somehow different.

To simulate the pressure waves with low CPU load, a cell is treated as 1D tube, so that the governing equations are 1D Euler equations with a source term as written below.

$$\frac{\partial}{\partial t} \begin{bmatrix} \rho \\ \rho u \\ e \end{bmatrix} + \frac{\partial}{\partial x} \begin{bmatrix} \rho u \\ \rho u^2 + p \\ (e + p)u \end{bmatrix} = \begin{bmatrix} 0 \\ S_2 \\ 0 \end{bmatrix} \quad (26)$$

The term “S2” indicates the momentum loss by the wall viscosity, which will be explained later. The rest of the source terms are 0, because the wall is assumed to be adiabatic and the region only in the cells is

solved by this equation. The solution scheme of both spatial and time integral was adopted as the same in 2D numerical simulation described in the previous section.

Because the real inner flow dynamics in a wave rotor cannot be regarded as 1D flow, three dominant factors have to be taken into account in this model, that is, “Gradual Passage Opening”, “Leak Flow”, and “viscosity”. The factors above have been recognized to have large influence on the wave rotor performance according to the experiments [22].

3.4.1.1 Gradual Passage Opening Effect

This effect comes from the relative rotation process that means the cells are gradually opened and closed to the ports, which brings about a large influence especially on the pressure wave generation. Figure 23 shows the illustration of the left end of a cell when it begins to be opened against a port. Here, the volumes at the end of the cells are divided as shown in this figure. Volume D corresponds to that at the boundary for the calculation of the equations (26) in a cell. Volume C corresponds to a port, which is supposed to be uniform and constant during the calculation. Volume B corresponds to the clearance region, which is exposed to a port, while Volume A is exposed to the end wall. To calculate the condition of Volume D, the flux between these volumes is calculated with the application of Riemann invariance [31], although the shear stress at the interface is not considered here.

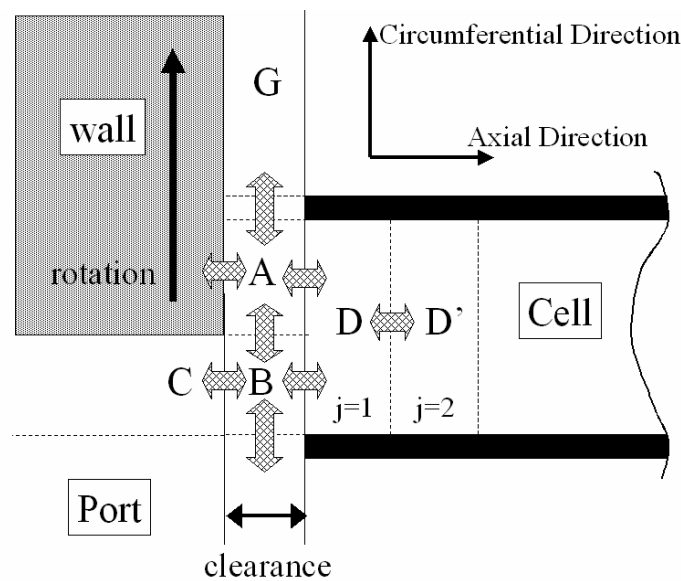


Figure 23: Modelling of Gradual Passage Opening and Leak Flow Effects [32].

3.4.1.2 Leak Flow Effect

The leak flow in the wave rotor operation indicates the flow in the clearance region between the rotor and the end wall, which correspond to the Volumes A, B and G in Figure 23. Here, this leak flow is considered to consist of two components, that are, towards the outside in the radial direction and to the circumferential due to the interaction between the neighboring cells.

To estimate the leak flow to the outside, the flux in the radial direction at Volumes A and B is calculated. Here, the outside condition is assumed to be constant and the same as the stagnation values in Air-LP. On the other hand, to simulate the interaction between the neighboring cells, the flux between Volumes A and G is calculated. Also, when the cell is completely closed, the flux between the neighboring cells on both sides has to be calculated.

3.4.1.3 Viscosity Effect

In estimation of the viscous gas effect, only the momentum loss by shear stress at the walls is considered here [35-37]. Therefore, the source term “S2” in the governing equations (26) becomes,

$$S_2 = -4 \frac{\tau_{wall}}{D_h}$$

Here, the shear stress τ_{wall} is modeled as written below according to the Rayleigh flow analogy.

$$\tau_{wall} = \frac{\mu U}{\sqrt{\pi \nu t}}$$

3.4.2 Verification of Numerical Modelling

To validate the numerical modelling above, the result is compared with that of 2D numerical simulation described in the section 3.3.2. In this comparison, the boundary condition and the design of ports and rotor are the same as those in the experimental facility for visualization. Figure 24 shows the comparison of the three-passage simulation of both numerical approaches. This figure shows the density distribution in the axial direction of the middle passage of the three. Here, $x=0$ corresponds to the gas side, which is opened to the Gas-HP, while $x=1$ corresponds to the air side, which is opened to the Air-HP. 2D results as the reference show the average value at each cross section.

As seen in this figure, the result of 1D numerical model shows excellent agreement with 2D result, in terms of the shock wave propagation. As for the primary shock wave, its pressure rise is not so sharp at the beginning of its propagation. One of the reasons is the gradual passage opening effect, and another is that the gas flows into the cell through the clearance before Gas-HP is opened to the cell. Here, the point is that the accumulation process of pressure waves has much influence on the propagation, and those effects can be considered in this 1D numerical model. As for the secondary shock wave, a little difference appears at its position and pressure ratio, although it is not serious in practice. It can be concluded that this numerical model is applicable for the wave rotor design procedure.

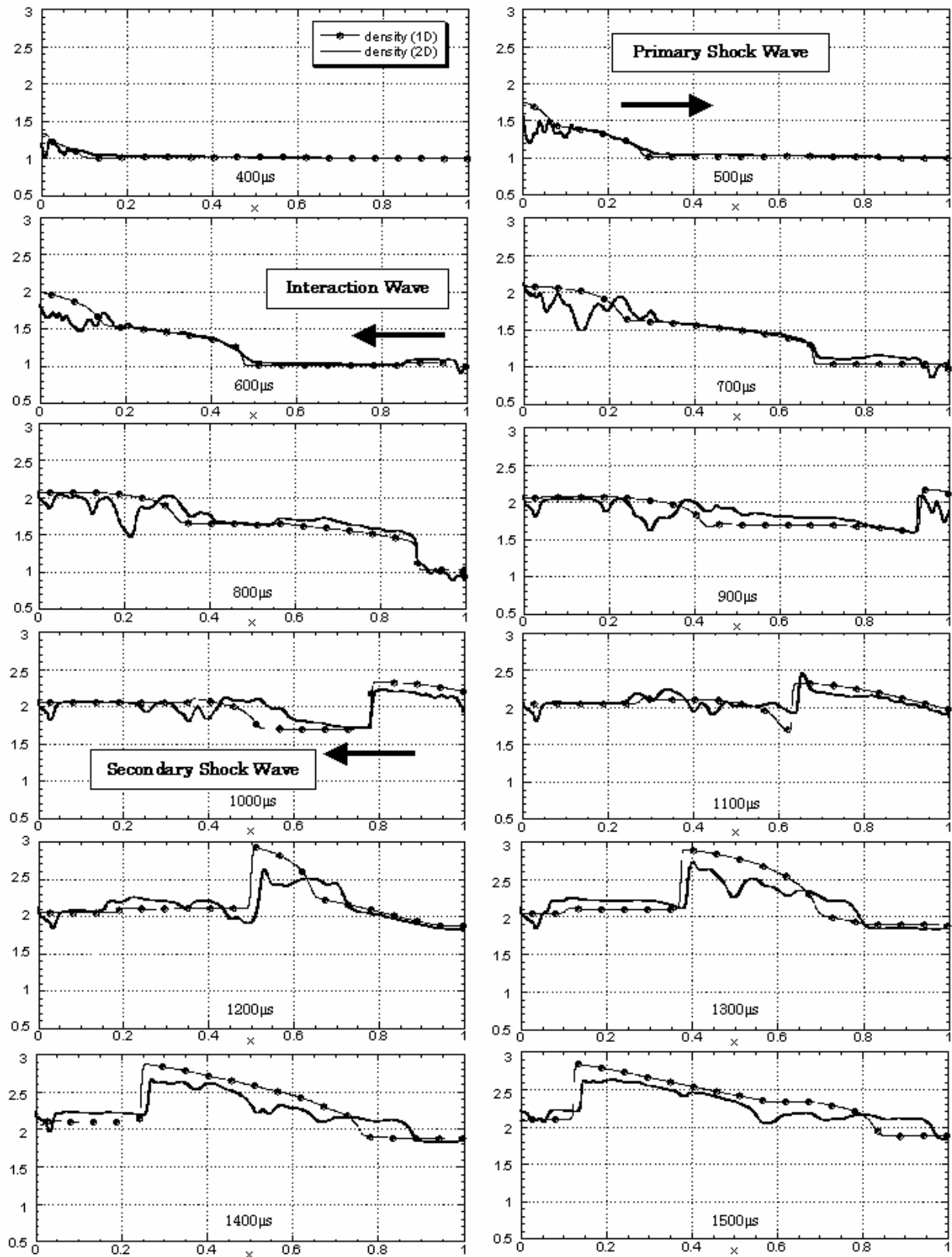


Figure 24: Comparison with 2D result [32].

3.5 Micro Wave Rotor

3.5.1 Design

With the present 1D numerical model, a wave rotor for kW size ultra-micro gas turbines was designed in reference to the NASA wave rotor [17]. This micro wave rotor is shown in Table 15 and Figure 25. Here, the pressure ratio of the baseline gas turbine was assumed to be 3.0, and the total temperature of Air-LP to be 440K.

Table 15: Condition in the Ports

	Gas-HP	Air-LP	Air-HP	Gas-LP
P_0 [atm]	9.2	3.0	10.1	3.7
T_0 [K]	1248	440	907	973

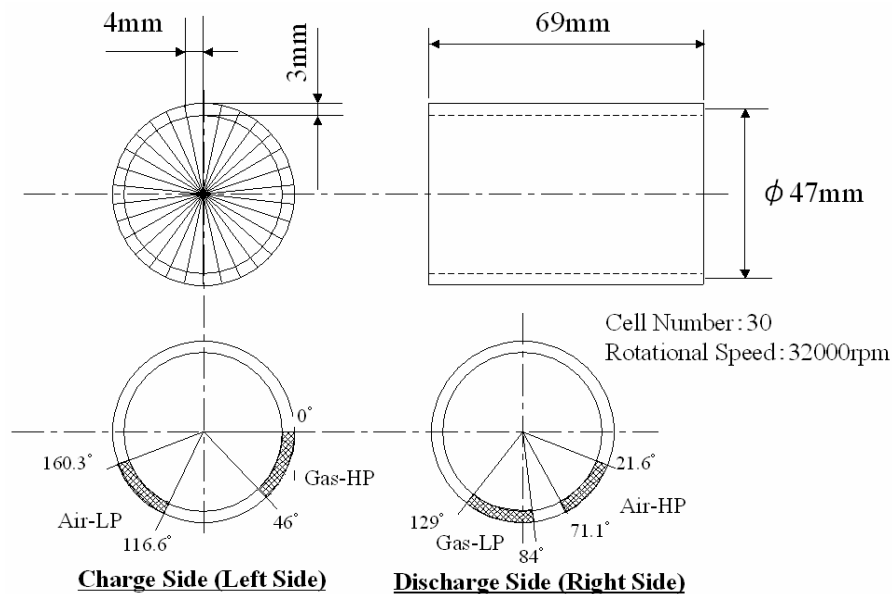


Figure 25: Design Particular of Micro Wave Rotor [32, 33].

To compare this design with other wave rotors, three non-dimensional parameters for the dominant factors are introduced as follows, in accordance with the experimental work of NASA G.R.C. [22, 23].

$$\text{Gradual Passage Opening } T = \frac{\text{Passage Opening Time}}{\text{Wave Travel Time}} = \frac{b}{w} \cdot \frac{a}{L}$$

$$\text{Viscosity } F = \frac{\sqrt{\nu \cdot L / a}}{D_h}$$

$$\text{Leak Flow } G = \frac{2\delta}{H}$$

Nomenclature

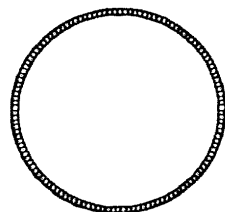
a : sound speed b : cell width w : tangential velocity of the rotor
 ν : kinematic viscosity D_h : hydraulic diameter of the passage
 δ : clearance H : cell height

As seen here, the parameter for gradual passage opening means the ratio of passage opening time and pressure wave travelling time in a cell, which is normally less than 1.0. The parameter for the viscosity effect means the loss by the wall shear stress, and other factors, such as mixture loss at the contact surface of gas and air, are not taken into account. As for the parameter of leak flow effect, it shows the area ratio of the cell cross-section and the clearance region at both end of the cells.

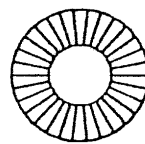
Table 16 shows a summary of the previous experiments, in which available geometrical particulars are listed in some details with sketches underneath. In this comparison, larger parameter value yields larger performance loss in each factor. As seen in this table, viscosity and leakage effects of this micro wave rotor will bring larger performance loss compared to others, which seems to be similar to the tendency of conventional turbo machinery miniaturization.

Table 16: Summary of Geometries and Parameter Values in Experiments

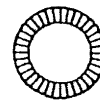
	NASA (3 port)	NASA & Allison	Kentfield	G.E.	Compresx® (ABB)	Equipment for Visualization (this study)	Micro Wave Rotor (this study)
Length [m]	0.46	0.152	0.28	0.3	0.0932	0.186	0.069
Mean Radius [m]	0.15	0.0815	0.074	0.058	0.0048	0.06	0.02325
Number of Passages	130	52	30	36	34	1 or 3	30
Cell Width [m]	0.007	0.00875	0.015	0.01	0.009	0.008	0.004
Cell Height [m]	0.0102	0.0223	0.0559	0.0231	0.01	0.016	0.003
Clearance [mm]	variable	0.1	0.18	0.64	0.15	0.5	0.1
Rotating Speed [rpm]	4000	16800	6000	19000	14000	4200	32000
T	(0.082)	0.19	(0.39)	(0.098)	0.467	0.55	0.31
F	(0.017)	0.0037	(0.0046)	(0.0081)	0.0067	0.0084	0.012
G	variable	0.0090	0.0064	0.055	0.030	0.063	0.067



NASA (3-Port)



Kentfield



G.E.

Figure 26 shows the numerical result of this micro wave rotor, which was calculated with the 1D numerical model. The contour shows the total temperature distribution, which corresponds to the wave diagram of Figure 14. As seen in this figure, the inner flow dynamics seems to be almost the same as the wave diagram, therefore this design is appropriate as a wave rotor.

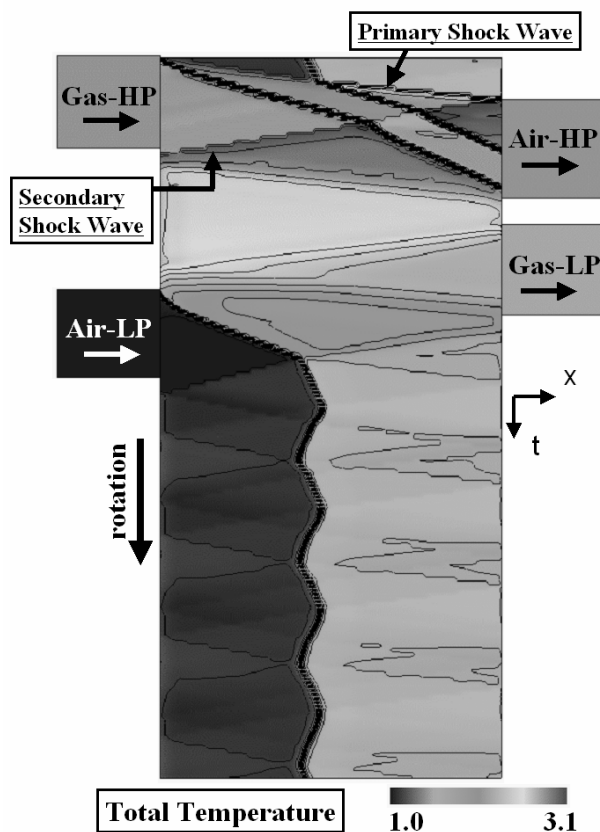


Figure 26: Inner Flow Dynamics of Micro Wave Rotor (Total Temperature) [32, 33].

3.5.2 Port Adjustment

According to the wave diagram (Figure 14), the distance between the Air-HP and Gas-LP is not strictly decided by the pressure wave propagation, and it is generally considered that this distance should be long enough so that the condition in the cell becomes stable. Therefore, two different port arrangements were calculated and compared as shown in Table 17. That distance of Case 1 is short, which was already shown in Figure 25, while that of Case 2 is much longer than Case 1.

Table 17: Ports' Configurations

	Case 1	Case 2
Gas-HP [degree]	0 – 46	0 – 46
Air-LP [degree]	116.6 – 160.3	296.1 – 339.8
Air-HP [degree]	21.6 – 71.1	21.6 – 71.1
Gas-LP [degree]	84 – 129	263.5 – 308.5

Figure 27 compares the total pressure contours between two cases of the port distance, in which the clearance is also changed into 0.0, 0.1 and 0.2 mm, respectively. Here, the pressure, when the cell starts to be opened to Gas-LP, should be noticed, because the pressure rise of Gas-LP corresponds to the contribution to the whole cycle.

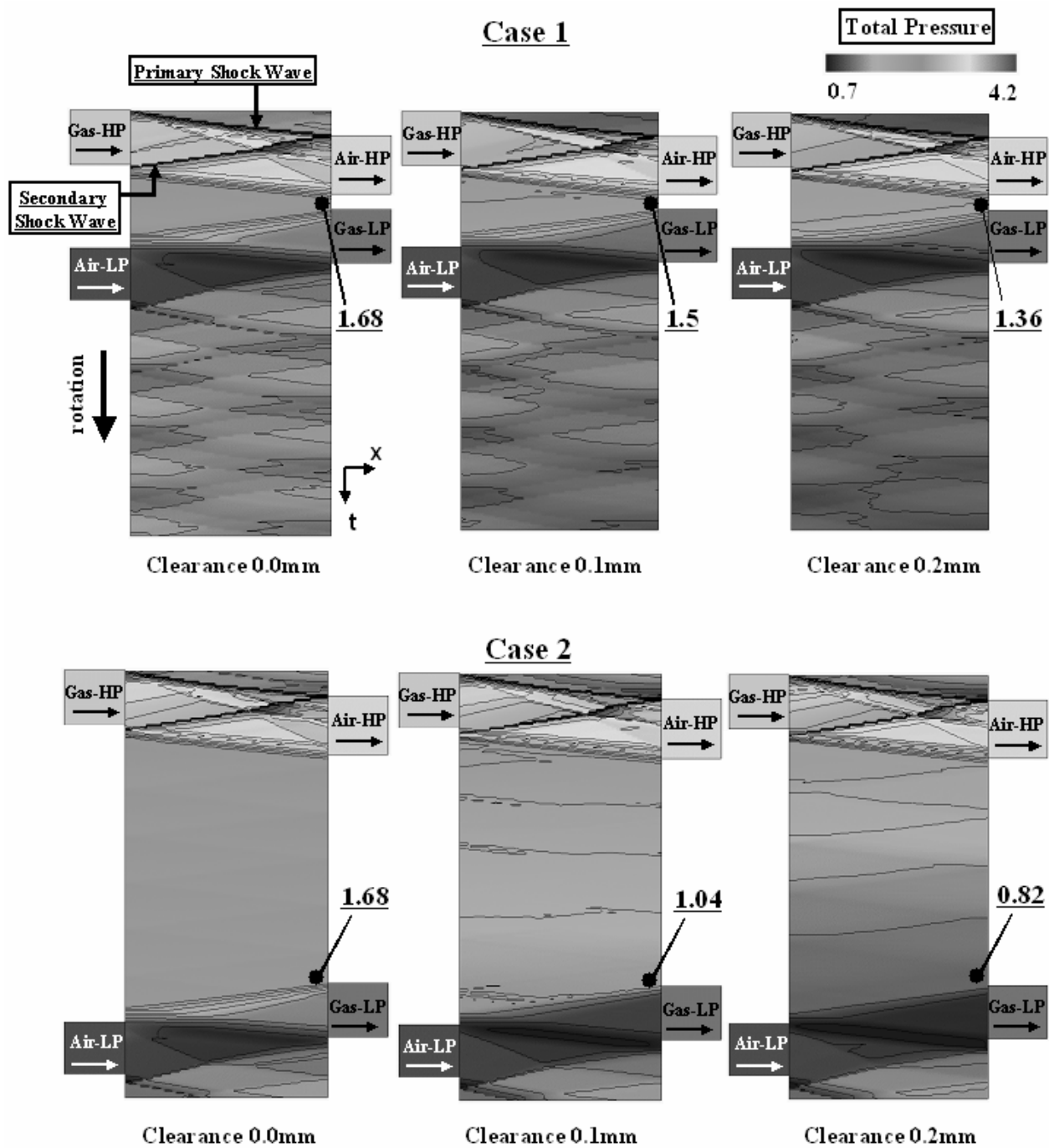


Figure 27: Comparison of Different Port Arrangements with Clearance Value [32, 33].

As seen in this figure, there seems to be no difference between Case1 and Case2, when the clearance is 0.0mm. And the pressure drops according to the increase of clearance, because the leak flow between Air-HP and Gas-LP increases. Table 18 shows the ratio of the leak flow and the mass flow in the Air-LP. Here, only qualitative discussion is possible, because the surrounding condition of the rotor is considered to be constant in the present simulation, despite the pressure in the rotor cavity will be changed by the leak flow. This result shows that the Case1 of 0.2mm clearance is better than the Case2 of 0.1mm clearance. This means that the leak flow is mainly generated between the high-pressure and the low-pressure ports at

either side. Therefore, the shorter the distance between Air-HP and Gas-LP, the better the performance will become. In the design of ultra-micro wave rotors, this tendency will be intensified, because the leak flow effect will have larger influence on the performance than in the conventional turbo machine. From all these consideration, the optimized distance between Air-HP and Gas-LP is set a cell width at the minimum, because a cell should not be opened to two ports at the same instance.

Table 18: Leak Mass Flow Rate

Clearance [mm]	Leak Mass Case1	Flow Rate [%] Case2
0.0	0.0	0.0
0.1	25.8	42.0
0.2	38.0	56.5

3.5.3 Development of Test Rig

Based on the design above, a micro wave rotor test model was built in this study [39], as shown in Figure 28. As seen in Figure 29, two compressors were used here to supply air to Gas-HP and Air-LP. In this experiment, only the pressure ratio was achieved, therefore the effect of high temperature was not considered. Gas-HP and Air-LP were kept almost 0.303 and 0.11MPa, respectively, while Air-HP and Gas-LP were opened to the atmosphere with valves. Each valve was set to keep high or low pressure at the optimal rotational speed, though it was not controlled actively during the experiment. The rotor was driven by an electric inverter motor, and the rotational speed was measured by an optical sensor.

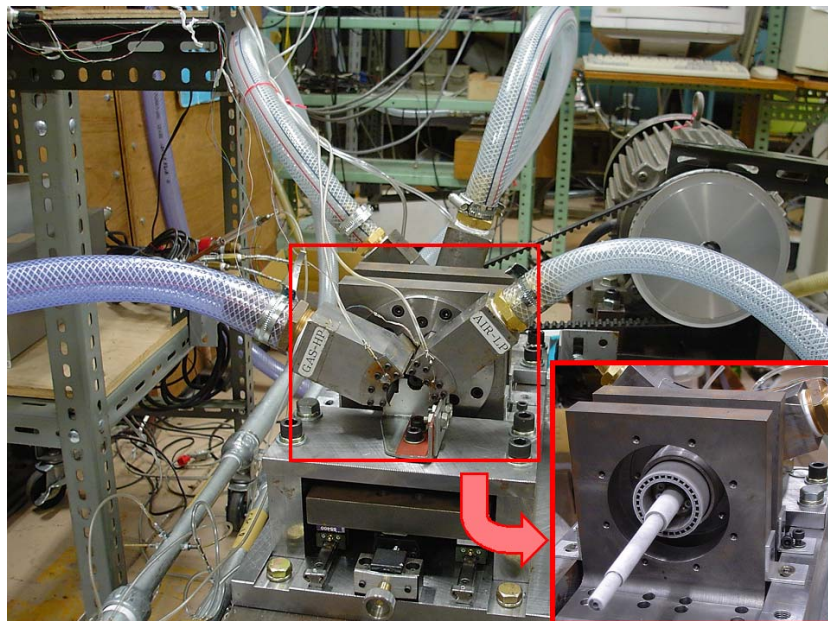


Figure 28: Micro Wave Rotor Test Model [39].

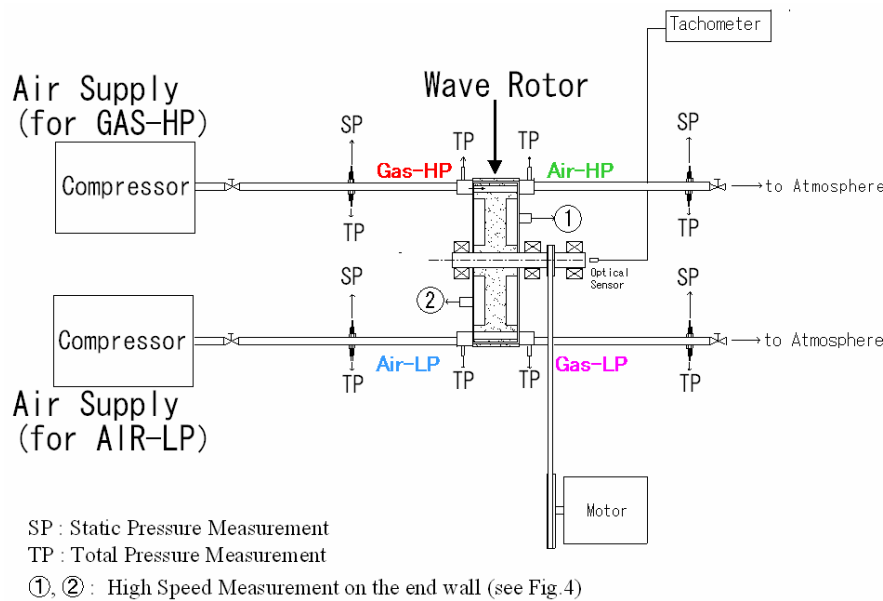


Figure 29: System Arrangement of Micro Wave Rotor [39].

As for the measurement, static and total pressure were measured in the duct of upstream or downstream of each port to yield the mass flow rate. Also, the total pressure in each port was measured for the valve control, as well as for the experimental data. In this experiment, high-speed pressure measurement at the end wall was introduced to obtain the data for the pressure wave arrival. The measuring point of no.1 was made just before the Air-HP opening, and that of no.2 just before the Air-LP opening, as already indicated in Figure 14.

3.5.4 Test Run with Cold Air

Figure 30 shows the plot of mass flow rate in each port versus rotational speed. As seen in this figure, the characteristic of mass flow rate in each port changes around the rotational speed of 300Hz (=18000rpm). According to the results of 1D numerical model (Figure 31), the optimum rotational speed in this operating condition is 300Hz, judging from the arrival timing of the primary and secondary shock waves at the cell ends. This numerical result can be verified by the high-speed pressure measurement at No.1 (Figure 32). The peak of oscillating pressure reaches more than 0.3MPa by the reflection of primary shock wave, when the rotational speed is 200Hz. On the contrary, when the rotational speed is 400Hz, the pressure peak is less than 0.15MPa, therefore shock wave reflection does not happen in this case. Here, it is noted that the optimum rotational speed of 300Hz is different from the setting shown in Figure 25, because it is much affected by the sound speed, that is, the temperature distribution, whereas the temperature in each port was room temperature in this experiment.

In the expansion process, the most important point is the opening timing of Air-LP. Air-LP should be opened to the cells when the pressure at the left end becomes low enough to induce fresh air from Air-LP. The pressure in the cells is decreased by the expansion wave generated by the Gas-LP opening, therefore the slower rotation brings lower pressure as shown in Figure 31.

As seen in Figure 30, the inflow mass flow rate in Air-LP could not be observed presently at any rotational speeds, whereas the average pressure value in the cells is clearly less than the pressure in Air-LP at 200Hz, according to the high-speed pressure measurement at No.2 (Figure 33). Two possibilities may be reasoned for this situation. One is that the expansion wave generated by Gas-LP opening is too weak. The other is that the cells may induce the air from the surroundings through the clearance region, not from Air-LP.

In any case, the crucial point seems to be the clearance, therefore its effect should be as much as eliminated for proper operation of expansion process.

Moreover, in this micro wave rotor, the leak flow effect can be a serious problem, as described previously in relation to G parameter in Table 16. Figure 34 shows the mass flow rate of leakage, which is calculated from the balance between the four ports. As shown in this plot, the leakage mass flow rate depends mainly on the clearance value itself, while it is not much affected by the rotational speed. Also, the value itself is excessive compared to the mass flow rate of Gas-HP. Therefore it is necessary to make further efforts to reduce the leakage in practice.

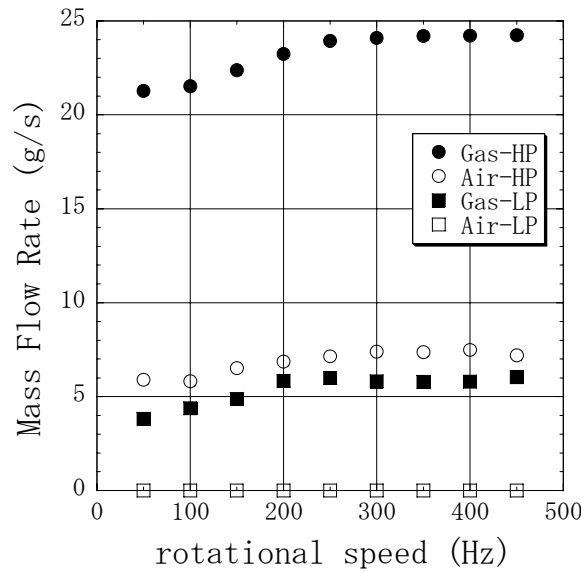


Figure 30: Mass Flow Rate versus Rotational Speed [39].

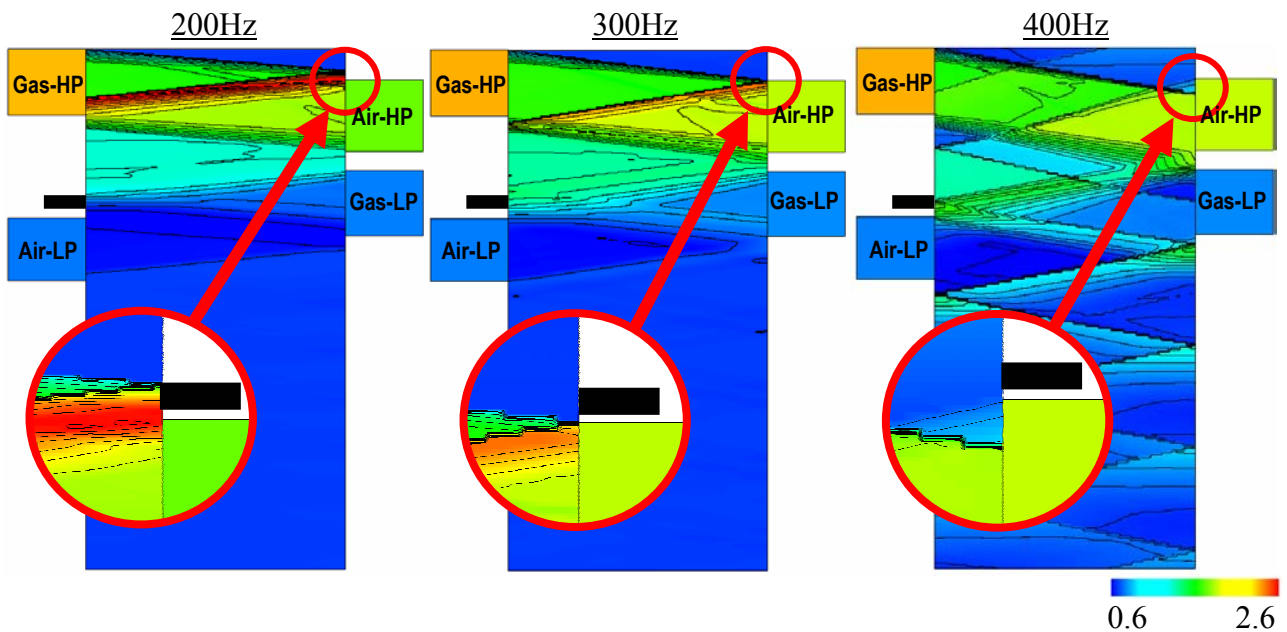


Figure 31: Calculated Pressure Wave Dynamics at Each Rotational Speed [39] (Total Pressure Distribution).

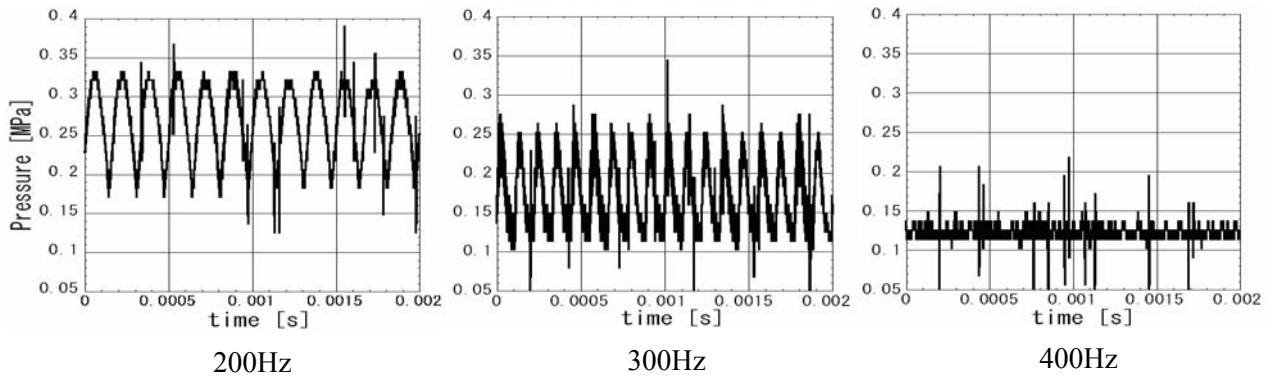


Figure 32: High Speed Measurement of Pressure at No.1 Point on the End Walls [39].

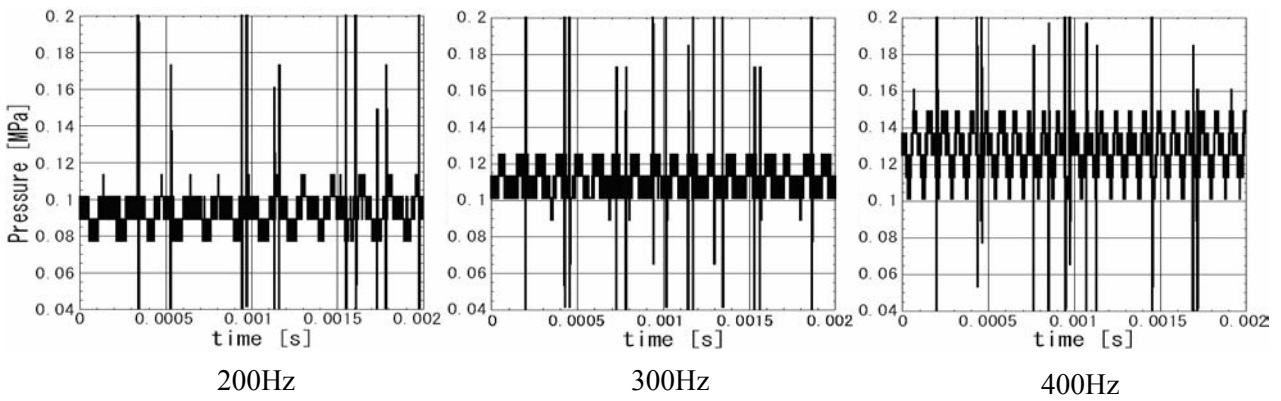


Figure 33: High Speed Measurement of Pressure at No.2 Point on the End Walls [39].

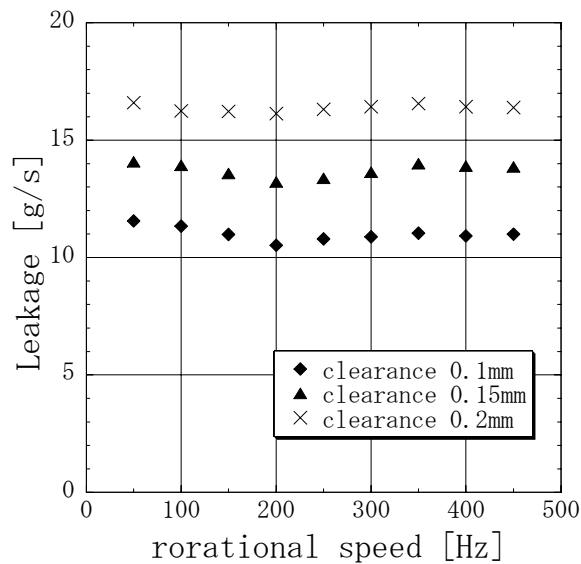


Figure 34: Mass Flow Rate of Leakage [39].

3.6 Flow Visualization in a Micro Tube [40]

3.6.1 Test Facility for Visualization of Micro Tube

In miniaturizing wave rotors, the viscous effect becomes serious as well as the leakage effect, because the rotational speed is mainly decided by the cell length. In other words, the rotational speed can be decreased by lengthening the cells, while it is decided the peripheral speed of the rotor in the case of conventional turbo machinery. This is one of the advantages of wave rotors in the miniaturisation, but the longer cell leads to be larger viscous loss. Therefore, it is significant to investigate the viscous effect in a micro tube to know the limit of its length.

In the present study, an experimental equipment for micro tube visualization was built with introducing the same concept of the original equipment described in the section 3.3.1. Figure 35 shows a schematic and photograph of the equipment. As shown here, a rotor with inlet and exhaust ports is rotating, but the buffer chamber to supply high pressure air from a screw compressor is fixed. The inlet port perforated so that the high pressure air flows into the test section through this inlet port, while the exhaust port is a hollow and the air is discharged in the radial direction. The total pressure in the buffer chamber is controlled with a valve and is monitored with a pressure gauge. Between the buffer chamber and the cell, the rotor with ports is installed. The rotor is driven by an electric motor whose speed is monitored with an optical pickup. The rotor has two inlet and two exhaust ports. The inlet port opening is 11 deg and the pitch is 180 deg. The pressure in the buffer chamber and rotational speed is set as 2.5MPa and 5,000rpm, respectively.

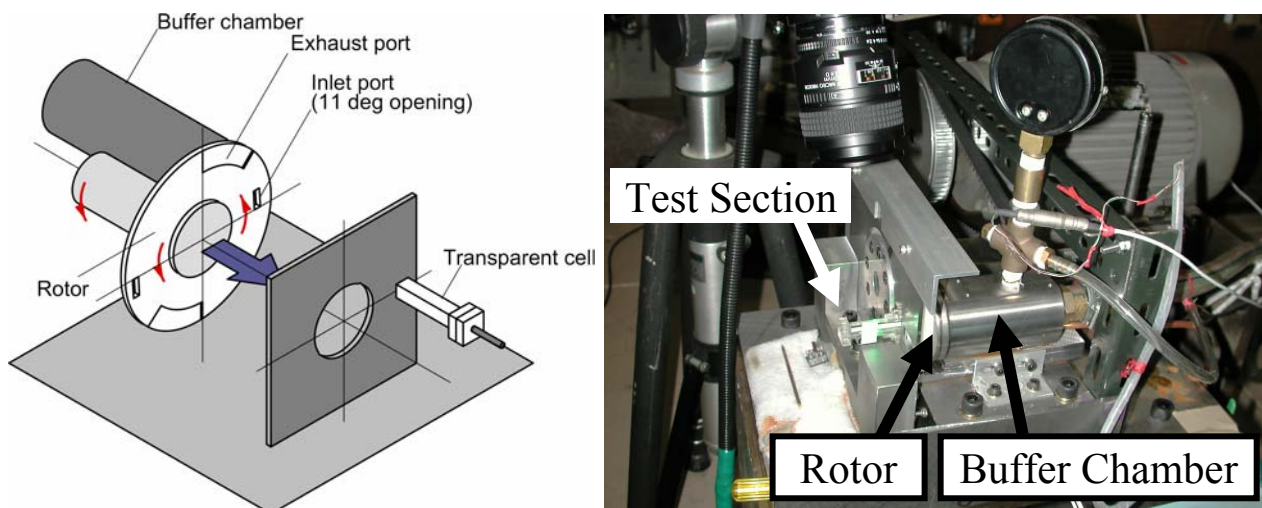


Figure 35: Equipment for Micro Tube Visualization.

Figure 36 shows the transparent cell. The cross-section is 3 x 3 mm rectangular tube, whose length is 42mm. At the downstream end of the cell, a pressure transducer is installed to measure the total pressure inside the cell. The origin of the coordinate system is set at the centre of the cell entrance. The x, y and z coordinate are set along the streamwise, transverse and spanwise directions.

In this experiment, a Laser Doppler Anemometry (LDA) is employed for the direct measurement of velocity distribution in the cell, as well as the high speed pressure measurement at the cell end. In this LDA measurement, the light source is a CW Nd: YAG laser (532nm), and ethanol droplets are seeded as scattering particles. Measurement duration of one run is 15 second. Before a run, 10cc liquid ethanol is supplied into the buffer chamber and is blasted by the high-pressure air. The laser beams of the LDA

measurements intersect at the centre axis of the cell and the x (streamwise) velocity component is measured. The LDA measurement positions are indicated in the side view of Figure 36.

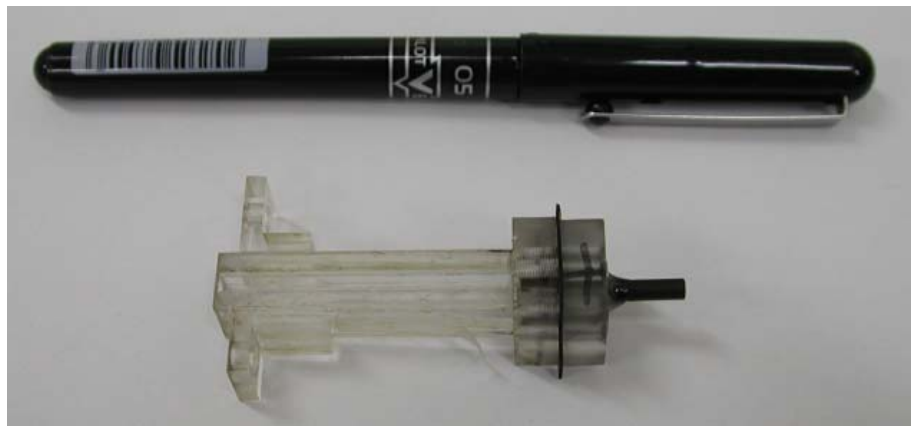
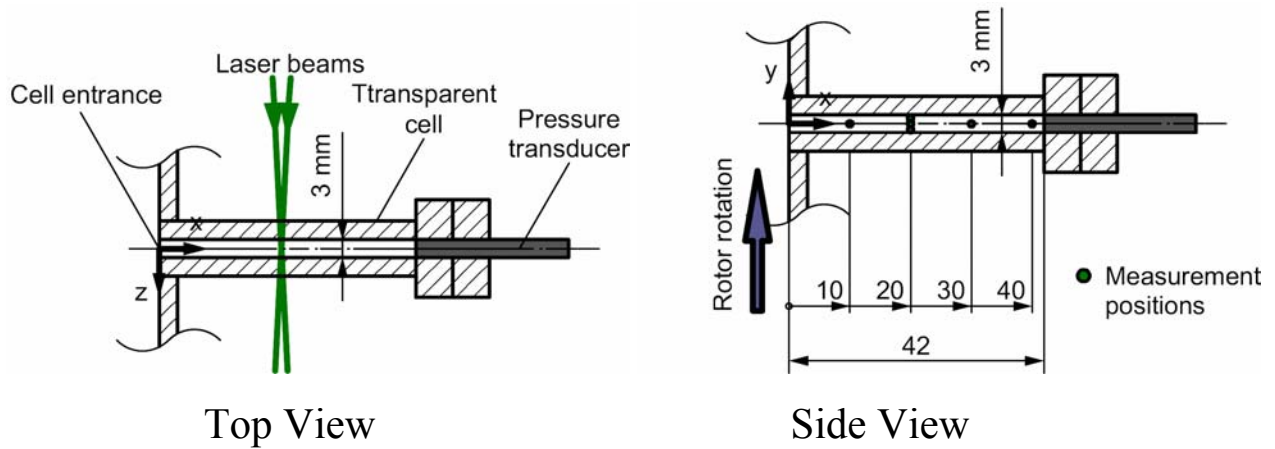


Figure 36: Test Section.

The spatial resolution of an LDA is determined by the size of the laser intersection volume, and the smaller intersection volume is demanded for such a small test section. On the other hand, the intersection angle should be less than 3 degree (half angle) with considering the velocity range, while it yields longer intersection volume. Therefore in this study, beam expanders are used to decrease the beam waist diameter, and the size of intersection volume is reduced to a sub-millimeter size (about 0.6×0.03 mm) in consequence.

3.6.2 Results and Discussion

Figure 37 shows the results of the velocity and total pressure measurements inside the cell. The plots (a) to (d) show the results of the LDA measurements at $x = 10, 20, 30$ and 40 mm with $y = 0$ (at the center axis), respectively. The plot (e) shows the result of the total pressure measurement at the cell end ($x = 42$ mm). In these plots, the horizontal axis shows the rotor angle, while the vertical ones show the velocity or pressure. The results are discussed according to the rotor angle.

During 0 to 10 degree, the fluid is suddenly accelerated by the primary shock wave, and the pressure rise is also observed in the pressure trace. The propagating velocity of Primary Shock Wave is 4.0×10^2 m/s, which is calculated from the gradient of its characteristic line, while the theoretical value of a normal shock wave for the same pressure ratio is 5.1×10^2 m/s. Therefore, the primary shock wave seems to be still compression wave, because of the gradual passage opening and the short cell length. This explanation is consistent with the fact that it takes certain duration (around 3 degree) to increase in the velocity. After

acceleration, the fluid is decelerated by the secondary shock wave, while the pressure at the cell end increases by the shock wave reflection.

During 10 to 30 degree, the velocity of the fluid is negative, and the total pressure at the cell end decreases gradually. Here, the inlet port starts to close around the rotor angle of 10 degree. Therefore, the negative velocity near the cell inlet corresponds to the discharge or leakage to the surroundings.

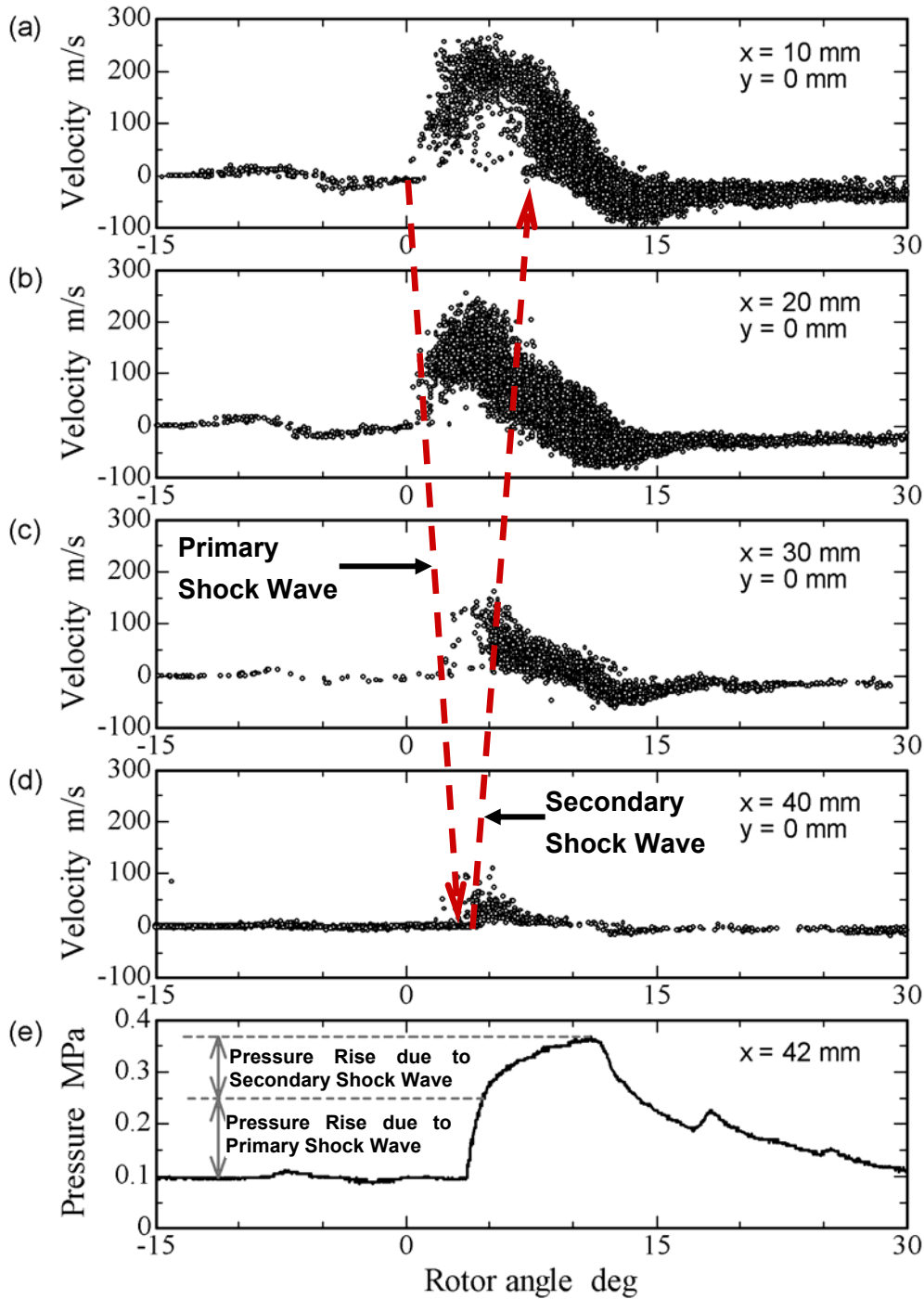


Figure 37: Velocity and Total Pressure Histories.

On the other hand, the comparison in the y direction is shown in Figure 38. Here, it must be considered that the maximum velocity reaches more than 200m/s in the charging process with the primary and secondary shock waves, and it also reaches about 100m/s in the discharging process, in such a tiny tube. Also, the maximum velocity at each measuring point seems to be almost the same, so that it can be considered that the boundary layer thickness is less than 0.5mm, although the non-dimensional parameter of viscosity “ F ” is 0.14, which is relatively large (see Table 16). From this result, the design of larger parameter value of “ F ” seems to be possible for the shock wave propagation, but the viscosity brings performance loss with certainty according to the experiments [22, 23], and further investigation is necessary to investigate the loss mechanism of viscosity effect.

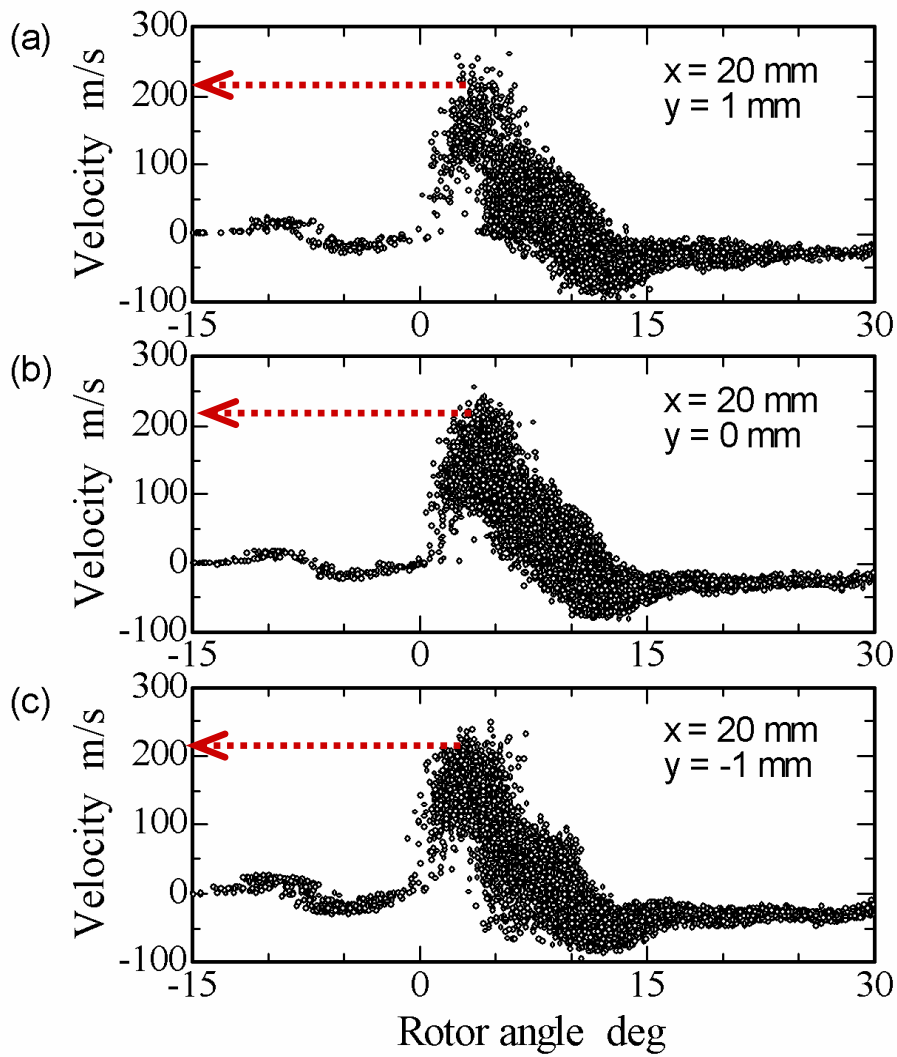


Figure 38: Velocity Comparison in the Circumferential Direction.

3.7 Further Miniaturization for Power MEMS

When a wave rotor is fabricated by MEMS technology, the cell length is restricted by its depth limitation, which is currently about 0.5mm. When the port arrangement is supposed to be the same as the micro wave rotor described above, the cell length of 0.5mm brings about 4×10^6 rpm, which is doubled of the rotational speed of Power-MEMS turbine, although this can be improved by the arrangement of ports.

In any case, the rotational speed will be extremely high, and this yields the same difficulty of high-speed rotation as in Power-MEMS turbine.

One of the solutions for this limitation is to align the cells in the radial direction, instead of the axial direction. Figure 39 shows the rotor fabricated on a glass disk by MEMS technology. The inner and outer diameters of the disk are 60 and 100 mm, and the passage height and width are 0.6mm and 4.0mm, respectively. According to such an idea, the cell length can be decided with more freedom, which brings slower rotational speed, although the limitation is imposed on the cell height, which yields larger friction loss. As a result, the cell length is restricted by the friction loss factor, so that it is significant to investigate this point well.

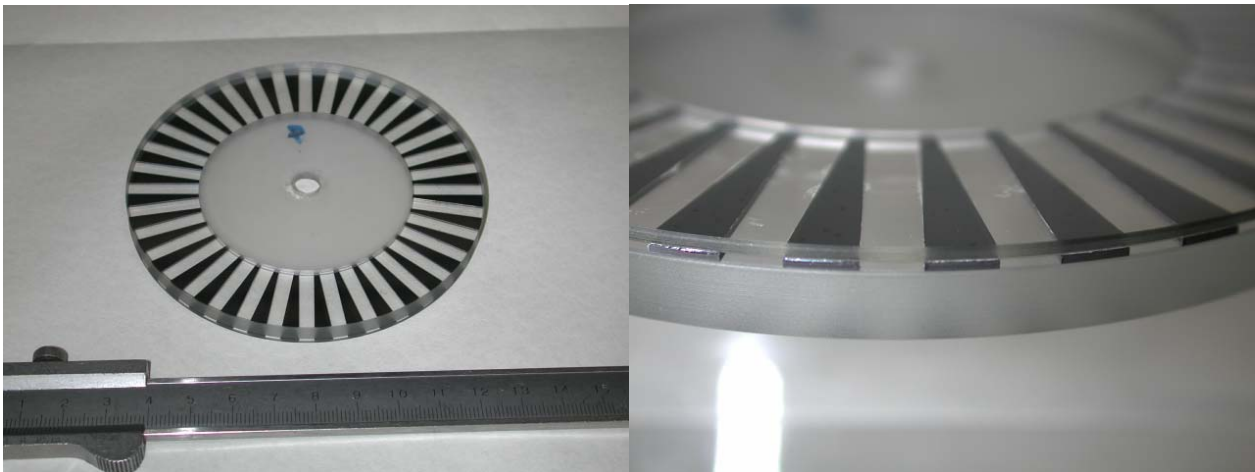


Figure 39: Radial Wave Rotor.

The design of this radial wave rotor is more difficult than the conventional axial wave rotors, because the cell length concerns with the rotor diameter. In addition, the radial flow requires or makes much rotational torque, which may yield instability of rotation. Another difficulty will be found also in the port design of inner side of the disk because of its less space, so that it is not clear whether this idea has better prospects or not. This idea is also suggested as “Wave Discs” for micro gas turbines in the references [41, 42], in which some other possibilities are suggested, such as cambered cell wall, internal combustion, and so on.

3.8 Summary

Wave rotor technology was introduced to improve UMGT performance.

First of all, cycle analysis was performed to discuss the impact of wave rotor topping cycle on micro and ultra-micro gas turbine. In the case of ultra-micro gas turbine, the benefit was much affected by the heat transfer in the mixing channel. If the thermal insulation of mixing channel were perfect, the performance gain of wave rotor topping reached more than 40%. In case of a little larger micro gas turbine, the improvement is thus expected more promising and attractive.

In the next section, the pressure wave dynamics in the passages were discussed based on the results of 2D numerical simulation and experiment including visualization of shock waves.

Depending on the investigation inner flow dynamics above, a simple 1 dimensional numerical model was developed to aid the design procedure of wave rotors. These numerical models were verified carefully with 2D numerical results so as to simulate the pressure wave dynamics precisely with low CPU load.

With this numerical model, a design of a micro wave rotor for micro gas turbines was made with optimizing the ports' arrangement to decrease the leakage effect. This micro wave rotor was built and its test run by using cold air was carried out and some basic comprehension on the pressure wave dynamics and operating characteristics were derived.

For further miniaturization, it is significant to investigate the viscous effect on the inner flow dynamics. A transparent tiny cell was employed to measure the fluid velocity by Laser Doppler Anemometry method. In this experiment, it was observed that the boundary layer is not much developed in the compression process.

At last, a new type of wave rotor was suggested to reduce its rotational speed, but it has more difficulty.

4. CONCLUDING REMARK

A methodology for precise consideration upon global energetic links between localized heat transfer has been demonstrated in a concrete application form by employing MIT Power-MEMS turbine as a detailed example modelling, wherefrom several important findings were pointed out, concerning measures to increase output power at UMGH design base.

An innovative use of wave rotors for a topping thermodynamic cycle was also explained, exploring miniaturization as a micro wave rotor.

Successful UMGH development as well as system integration of components such as a wave rotor requires the technology beyond our present knowledge about low Re number aerodynamics and heat transfer, in particular, synthesis of local heat balances depending upon the design architecture. The last subject will be certainly fit for a research field needing advanced computer-aided designing process.

ACKNOWLEDGEMENTS

Hot Button study was initiated at first by ONERA and developed with the participation of students from Ecole Centrale de Nantes, INSA de Rouen and Ecole des Mines de Paris. Further applications of Hot Button software were performed with a help of Mrs. Luc Bouhali from ONERA and with a support of the SPAé from DGA (thanks to M. Cueille). This work was supported by NEDO International Joint Research Project on Energy and Environment, entitled "Practicing research of button sized gas generators" in FY2001 and "Leading R&D to practice UMGH" in FY2002-2003. The first authors also thank for a support of 21COE Mechanical Systems Innovation, Univ. of Tokyo.

REFERENCES

- [1] Epstein, A.H., et al., "Micro-Heat Engines, Gas Turbines, and Rocket Engines---The MIT Microengine Project---," 28th AIAA Fluid Dynamics Conference, 4th AIAA Shear Flow Control Conference, AIAA 97-1773, 1997.
- [2] Y. RIBAUD. Internal heat mixing and external heat losses in an ultra microturbine, IGTC 2003 TOKYO OS-109.
- [3] A.H. EPSTEIN. Millimeter scale, MEMS gas turbine engines, ASME GT-2003-38866.
- [4] Y. GONG "et al ". Aerothermodynamics of Turbomachinery. ASME GT 2004-53877.
- [5] J.M. OWEN and R.H. ROGERS. Flow and heat transfer in rotating-Disc systems, RSP1989.

- [6] FRECHETTE L.G. .Assessment of viscous flows in high speed micro rotating machinery for energy conversion applications, Proceedings of ASME IMECE'01.
- [7] FRECHETTE L.G. “et al.”. An electrostatic induction micromotor supported on gas lubricated bearings, Technical Digest, MEMS 2001, p. 290.
- [8] KÖSER H. and LANG J.H... 2001. Modeling a high power density MEMS magnetic induction machine. M.I.T.. Modeling and simulation of microsystems, ISBN 0-9708275-0-4.
- [9] R.A VAN DEN BRAEMBUSSCHE, A.A. ISLEK, Z. ALSALIHI. Aerothermal optimization of micro gas turbine compressor including heat transfer. IGTC 2003 TOKYO OS-101.
- [10] Tatsuo ONISHI “et al”. Numerical design and study of a MEMS based microturbine. ASME GT 2005 68168, à paraître.
- [11] Toshio MASHIMO “et al” Effects of Reynolds number on performance characteristics of a centrifugal compressor. ASME71GT25.
- [12] O.E. BALJE. A guide to design, selection and theory, John Wiley and Sons.
- [13] J.P. JOHNSTON “et al”. Performance of a micro scale radial flow compressor impeller made in silicon nitride. IGTC 2003 TOKYO OS -110.
- [14] Koji OKAMOTO. Energetic study of an ultra microturbine. Post doctoral contribution. Private communication. Marc 2004.
- [15] Welch G.E., Jones S.M., Paxson D.E., “Wave Rotor-Enhanced Gas Turbine Engines”, NASA Technical Memorandum 106998, AIAA-95-2799, 1995.
- [16] Wilson J., Paxson D.E., “Jet Engine Performance Enhancement Through Use of a Wave-Rotor Topping Cycle”, NASA Technical Memorandum 4486, 1993.
- [17] Snyder P.H., Fish R.E., “Assessment of a Wave Rotor Topped Demonstrator Gas Turbine Engine Concept”, ASME Paper 96-GT-41, 1996.
- [18] Welch G.E., Paxson D.E., Wilson J., Snyder P.H., “Wave-Rotor-Enhanced Gas Turbine Engine Demonstrator”, NASA / TM-1999-209459, 1999.
- [19] Fatsis A., Ribaud Y., “Thermodynamic analysis of gas turbines topped with wave rotors”, Aerospace Science and Technology, No. 5, pp. 293-299, 1999.
- [20] Akbari P., Muller N., “Preliminary Design Procedure for Gas Turbine Topping Reverse-Flow Wave Rotors”, IGTC2003 FR-301, 2003.
- [21] Wilson J., Fronck D., “Initial Results From the NASA-Lewis Wave Rotor Experiment”, AIAA-93-2521, 1993.
- [22] Wilson J., “An Experimental Determination of Losses in a Three-Port Wave Rotor,” Journal of Engineering for Gas Turbine and Power, Vol. 120, pp. 833-842, 1998.
- [23] Wilson J., Fronck D., “Initial Results From the NASA-Lewis Wave Rotor Experiment”, AIAA-93-2521, 1993.

- [24] Bilgin M., Keller J.J., Breidenthal R.E., “Ignition and Flame Propagation Process with Rotating Hot Jets In a Simulated Wave Engine Test Cell”, AIAA-98-3399, 1998.
- [25] Okamoto K., “Wave Rotor Gasdynamics for an Aeropropulsion System”, ICAS PROCEEDINGS 2000 No. 7.3.4, 22nd INTERNATIONAL CONGRESS OF AERONAUTICAL SCIENCES, Sep. 2000.
- [26] Okamoto K., Nagashima T., Yamaguchi K., “Rotor-Wall Clearance Effects upon Wave Rotor Passage Flow”, ISABE2001-1222, 15th International Symposium on Airbreathing Engines, Sep. 2001.
- [27] Welch G.E., “Two-Dimensional Computational Model for Wave Rotor Flow Dynamics”, Journal of Engineering for Gas Turbine and Power, Vol. 119, pp. 978-985, 1997.
- [28] Welch G.E., “Two-Dimensional Numerical Study of Wave Rotor Flow Dynamics”. AIAA93-2525, 1993.
- [29] Larosiliere L.M., Mawid M., “Analysis of Unsteady Wave Processes in a Rotating Channel”, International Journal of Numerical Methods in Fluids, Vol. 21, pp. 467-488, 1995.
- [30] Larosiliere L.M., “Wave Rotor Charging Process: Effects of Gradual Opening and Rotation”, Journal of Propulsion and Power, Vol. 11, No. 1, January-February, 1995.
- [31] Toro E.F., “Riemann Solvers and Numerical Methods for Fluid Dynamics”, Springer, 1997, ISBN 3-540-61676-4.
- [32] Okamoto K., NAGASHIMA T., “A Simple Numerical Approach of Micro Wave Rotor Gasdynamic Design”, ISABE-2003-1213, 16th International Symposium on Airbreathing Engines, Aug. 2003.
- [33] Koji OKAMOTO, Toshio NAGASHIMA, Kazuo YAMAGUCHI, “Introductory Investigation of Micro Wave Rotor”, IGTC2003Tokyo FR-302, International Gas Turbine Congress 2003 Tokyo, Nov. 2003.
- [34] Paxson D.E., “A General Numerical Model for Wave Rotor Analysis”, NASA Technical Memorandum 105740, 1992.
- [35] Paxson D.E., “A Comparison Between Numerically Modeled and Experimentally Measured Loss Mechanisms in Wave Rotors”, AIAA-93-2522, 1993.
- [36] Paxson D.E., Wilson J., “An Improved Numerical Model for Wave Rotor Design and Analysis”, AIAA-93-0482, 1993.
- [37] Paxson D.E., Wilson J., “Recent Improvements to and Validation of the One Dimensional NASA Wave Rotor Model”, NASA Technical Memorandum 106913, 1995.
- [38] Fatsis A., Lafond A., Ribaud Y., “Preliminary analysis of the flow inside a three-port wave rotor by means of a numerical model”, Aerospace Science and Technology, No. 5, pp. 289-300, 1998.
- [39] Koji OKAMOTO, Kazuo YAMAGUCHI, Toshio NAGASHIMA, “Development of Micro Wave Rotor Test Model”, AJCPP2005-21021, Asian Joint Conference on Propulsion and Power 2005, Jan. 2005.
- [40] Mikiya ARAKI, Tsuneaki ISHIMA and Tomio OBOKATA, “Velocity Measurements inside a Micro Wave Rotor Cell”, Internal Communication, 2005 Feb.

- [41] Piechna J., Akbari P., Iancu F., Muller N., “Radial-Flow Wave Rotor Concepts, Unconventional Designs and Applications”, IMECE2004-59022, 2004.
- [42] Piechna J., “Wave Machines, Models and Numerical Simulation”, OFICYNA WYDAWNICZA POLITECHNIKI WARSZAWSKIEJ, ISSN 0137-2335.

Appendix 1

Input

General Data	Ambient Air Temperature (K)	288
	Ambient Air Pressure (Pa)	101325
	Specific Heat Ratio (air)	1.4
	r = Air Gas Constant	287.4
	r = Fuel vapor Constant	287.4
	Fuel Calorific Power (J/kg)	43100000
	Air Heat Capacity (J/kgK)	1004.5
	Heat Capacity of Burnt Gases (J/kgK)	1200
	Fuel Heat Capacity (J/kgK)	1620
	SiC Thermal Conductivity (W/mK)	500
	SiC Emissivity	0.87
Performance Data	Air Flow Rate (kg/s)	0.0001
	Initial Adiabatic Fuel Flow Rate (kg/s)	1.94E-06
	Polytropic Compressor Efficiency (Adiabatic Flow)	0.7
	Polytropic Turbine Efficiency (Adiabatic Flow)	0.6
	Rotor Speed (rad/s)	2.50E+05
	Combustion Efficiency (Adiabatic Flow)	0.95
	Combustor Exit Temperature (K)	1600
	Fuel Inflow Temperature (K)	288
	Initial Compressor Pressure Ratio (Adiabatic Flow)	3.9
Geometrical Data	Microturbine Outer Diameter (m)	0.012
	Microturbine Length (m)	0.003
	Blade Height (m)	2.00E-04
	Outer Radius of Compressor Rotor (m)	0.002
	Inner Radius of Compressor Rotor (m)	0.001
	Outer Radius of Turbine Rotor (m)	0.002
	Inner Radius of Turbine Rotor (m)	0.001
	Radius of Diffuser Inlet (m)	0.0023
	Radius of Diffuser Exit (m)	0.0027
	Radius of IGV Inlet (m)	0.0029
	Radius of IGV Exit (m)	0.0021
	Outer Radius of Combustor Chamber (m)	0.005
	Inner Radius of Combustor Chamber (m)	0.003
	Length of Combustor Chamber (m)	0.0025
	Channel External Radius (m)	0.005
	Channel Internal Radius (m)	0.0027
	Inter-Disk Space (m) (unused)	5.00E-06
Compressor Rotor Blade Number	8	
Turbine Rotor Blade Number	8	
Diffuser Blade Number	36	
IGV Blade Number	15	

Example of Results, Adiabatic Operation

Rotor Compressor Inlet (1)			Alpha (deg)	90	Static P (Pa)	98660
			Beta (deg)	75.2	Total P (Pa)	101325
	Merid. Mach Nbr	0.20	Meridional Speed	66	Static T (K)	286
	Tangential Mach Nbr	0	Tangential Speed	0	Total T (K)	288
	Relative Mach Nbr	0.76	Relative Speed	259	Static Rho (kg/m3)	1.201
	Mach Number	0.20	Omega * R	250	Total Rho (kg/m3)	1.224
			Speed (m/s)	66		
Rotor Compressor Exit			Alpha (deg)	3.2	Static P (Pa)	194154
			Beta (deg)	71.0	Total P (Pa)	395168
	Merid. Mach Nbr	0.06	Meridional Speed	24	Static T (K)	410
	Tangential Mach Nbr	1.06	Tangential Speed	430	Total T (K)	502
	Relative Mach Nbr	0.18	Relative Speed	74	Static Rho (kg/m3)	1.649
	Mach Number	1.06	Omega * R	500	Total Rho (kg/m3)	2.739
			Speed (m/s)	430		
Diffuser Inlet			Alpha (deg)	2.8	Static P (Pa)	234188
			Beta (deg)	#	Total P (Pa)	395168
	Merid. Mach Nbr	0.04	Meridional Speed	18	Static T (K)	432
	Tangential Mach Nbr	0.90	Tangential Speed	374	Total T (K)	502
	Relative Mach Nbr	#	Relative Speed	#	Static Rho (kg/m3)	1.885
	Mach Number	0.90	Omega * R	#	Total Rho (kg/m3)	2.739
			Speed (m/s)	374		
Diffuser Exit (2)			Alpha (deg)	17.8	Static P (Pa)	393463
			Beta (deg)	#	Total P (Pa)	395168
	Merid. Mach Nbr	0.02	Meridional Speed	11	Static T (K)	501
	Tangential Mach Nbr	0.07	Tangential Speed	34	Total T (K)	502
	Relative Mach Nbr	#	Relative Speed	#	Static Rho (kg/m3)	2.731
	Mach Number	0.08	Omega * R	#	Total Rho (kg/m3)	2.739
			Speed (m/s)	35		
IGV Inlet			Alpha (deg)	90	Static P (Pa)	394623
			Beta (deg)	#	Total P (Pa)	395168
	Merid. Mach Nbr	0.04	Meridional Speed	33	Static T (K)	1599
	Tangential Mach Nbr	0	Tangential Speed	0	Total T (K)	1600
	Relative Mach Nbr	#	Relative Speed	#	Static Rho (kg/m3)	0.858
	Mach Number	0.04	Omega * R	#	Total Rho (kg/m3)	0.859
			Speed (m/s)	33		
IGV Exit			Alpha (deg)	6.2	Static P (Pa)	217935
			Beta (deg)	#	Total P (Pa)	395168
	Merid. Mach Nbr	0.10	Meridional Speed	71	Static T (K)	1387
	Tangential Mach Nbr	0.90	Tangential Speed	650	Total T (K)	1600
	Relative Mach Nbr	#	Relative Speed	#	Static Rho (kg/m3)	0.547
	Mach Number	0.90	Omega * R	#	Total Rho (kg/m3)	0.859
			Speed (m/s)	653		
Rotor Turbine Inlet			Alpha (deg)	6.5	Static P (Pa)	203804
			Beta (deg)	66.8	Total P (Pa)	395168
	Merid. Mach Nbr	0.11	Meridional Speed	78	Static T (K)	1365
	Tangential Mach Nbr	0.95	Tangential Speed	682	Total T (K)	1600
	Relative Mach Nbr	0.28	Relative Speed	198	Static Rho (kg/m3)	0.519
	Mach Number	0.96	Omega * R	500	Total Rho (kg/m3)	0.859
			Speed (m/s)	687		
Rotor Turbine Exit (4)			Alpha (deg)	90	Static P (Pa)	82833
			Beta (deg)	35.3	Total P (Pa)	101325
	Merid. Mach Nbr	0.51	Meridional Speed	353	Static T (K)	1254
	Tangential Mach Nbr	0.00	Tangential Speed	0	Total T (K)	1316
	Relative Mach Nbr	0.63	Relative Speed	432	Static Rho (kg/m3)	0.230
	Mach Number	0.51	Omega * R	250	Total Rho (kg/m3)	0.268
			Speed (m/s)	353		

Compressor power (W)	21.489291
Turbine power (W)	35.80653037
Net Power (W)	14.31723937

Appendix 2

Aerothermodynamics Conditions for the Non-Adiabatic Micro-Turbine

Compression Rate				3.43				
Biot Number				0.018				
Specific Heat Ratio for Burnt Gases				1.31				
Brayton - Joule Cycle	1->2	Compression						
	2->3	Combustion at constant Pressure						
	3->4	Expansion						
1	Static Pressure (Pa)	98660		3 Combustion Chamber	Static Pressure (Pa)	347363		
	Total Pressure (Pa)	101325			Total Pressure (Pa)	347338		
	Static Temperature (K)	266			Static Temperature (K)	1600		
	Total Temperature (K)	268			Total Temperature (K)	1600		
	Static Mass per Unit Volume (kg/m ³)	1.201			Static Mass per Unit Volume (kg/m ³)	0.755		
	Total Mass per Unit Volume (kg/m ³)	1.224			Total Mass per Unit Volume (kg/m ³)	0.869		
2	Static Pressure (Pa)	344710		4	Static Pressure (Pa)	88151		
	Total Pressure (Pa)	347338			Total Pressure (Pa)	101325		
	Static Temperature (K)	771			Static Temperature (K)	959		
	Total Temperature (K)	773			Total Temperature (K)	991		
	Static Mass per Unit Volume (kg/m ³)	1.556			Static Mass per Unit Volume (kg/m ³)	0.320		
	Total Mass per Unit Volume (kg/m ³)	1.564			Total Mass per Unit Volume (kg/m ³)	0.356		
Rotor Compressor Inlet (1)	Alpha (deg)	90		Static P (Pa)	98660			
	Beta (deg)	75.2		Total P (Pa)	101325			
	Merid. Mach Nbr	0.20	Meridional Speed	66		Static T (K)	286	
	Tangential Mach Nbr	0	Tangential Speed	0		Total T (K)	288	
	Relative Mach Nbr	0.76	Relative Speed	259		Static Rho (kg/m ³)	1.201	
	Mach Number	0.20	Omega * R	250		Total Rho (kg/m ³)	1.224	
			Speed (m/s)	66				
Rotor Compressor Exit	Alpha (deg)	4.0		Static P (Pa)	193331			
	Beta (deg)	66.9		Total P (Pa)	347338			
	Merid. Mach Nbr	0.07	Meridional Speed	30		Static T (K)	507	
	Tangential Mach Nbr	0.95	Tangential Speed	430		Total T (K)	599	
	Relative Mach Nbr	0.17	Relative Speed	76		Static Rho (kg/m ³)	1.327	
	Mach Number	0.95	Omega * R	500		Total Rho (kg/m ³)	2.016	
		Speed (m/s)	431					
Diffuser Inlet	Alpha (deg)	3.9		Static P (Pa)	238419			
	Beta (deg)	#		Total P (Pa)	347338			
	Merid. Mach Nbr	0.05	Meridional Speed	26		Static T (K)	615	
	Tangential Mach Nbr	0.75	Tangential Speed	374		Total T (K)	685	
	Relative Mach Nbr	#	Relative Speed	#		Static Rho (kg/m ³)	1.348	
	Mach Number	0.75	Omega * R	#		Total Rho (kg/m ³)	1.763	
		Speed (m/s)	375					
Diffuser Exit (2)	Alpha (deg)	18.9		Static P (Pa)	344710			
	Beta (deg)	#		Total P (Pa)	347338			
	Merid. Mach Nbr	0.03	Meridional Speed	19		Static T (K)	771	
	Tangential Mach Nbr	0.10	Tangential Speed	55		Total T (K)	773	
	Relative Mach Nbr	#	Relative Speed	#		Static Rho (kg/m ³)	1.556	
	Mach Number	0.10	Omega * R	#		Total Rho (kg/m ³)	1.564	
		Speed (m/s)	58					
IGV Inlet	Alpha (deg)	90		Static P (Pa)	346771			
	Beta (deg)	#		Total P (Pa)	347338			
	Merid. Mach Nbr	0.05	Meridional Speed	36		Static T (K)	1532	
	Tangential Mach Nbr	0	Tangential Speed	0		Total T (K)	1532	
	Relative Mach Nbr	#	Relative Speed	#		Static Rho (kg/m ³)	0.788	
	Mach Number	0.05	Omega * R	#		Total Rho (kg/m ³)	0.789	
		Speed (m/s)	36					
IGV Exit	Alpha (deg)	6.7		Static P (Pa)	243575			
	Beta (deg)	#		Total P (Pa)	347338			
	Merid. Mach Nbr	0.08	Meridional Speed	53		Static T (K)	1160	
	Tangential Mach Nbr	0.68	Tangential Speed	452		Total T (K)	1262	
	Relative Mach Nbr	#	Relative Speed	#		Static Rho (kg/m ³)	0.731	
	Mach Number	0.69	Omega * R	#		Total Rho (kg/m ³)	0.957	
		Speed (m/s)	455					
Rotor Turbine Inlet	Alpha (deg)	6.9		Static P (Pa)	233406			
	Beta (deg)	24.3		Total P (Pa)	347338			
	Merid. Mach Nbr	0.09	Meridional Speed	57		Static T (K)	1136	
	Tangential Mach Nbr	0.72	Tangential Speed	474		Total T (K)	1249	
	Relative Mach Nbr	0.10	Relative Speed	63		Static Rho (kg/m ³)	0.715	
	Mach Number	0.73	Omega * R	500		Total Rho (kg/m ³)	0.967	
		Speed (m/s)	478					
Rotor Turbine Exit (4)	Alpha (deg)	90		Static P (Pa)	88151			
	Beta (deg)	44.4		Total P (Pa)	101325			
	Merid. Mach Nbr	0.42	Meridional Speed	256		Static T (K)	959	
	Tangential Mach Nbr	0	Tangential Speed	0		Total T (K)	991	
	Relative Mach Nbr	0.59	Relative Speed	358		Static Rho (kg/m ³)	0.320	
	Mach Number	0.42	Omega * R	250		Total Rho (kg/m ³)	0.356	
		Speed (m/s)	256					

Performance of the Non-Adiabatic Micro-Turbine

	Reynolds Number	Nusselt Number	h (W/m ² K)	S (m ²)	L (m)	Dynam. Viscosity	Th. Cond. (W/m/K)
	#	#	#	#	#	#	#
Inter Disk Front Cavity	10463	37.2	1024	9.425E-06	0.0020	3.832E-05	0.055
Compressor Rotor	14023	69.8	1513	1.737E-05	0.0015	2.265E-05	0.032
Vaneless Channel upstream of Diffuser	33686	108.2	2483	8.105E-06	0.0018	2.879E-05	0.041
Diffuser	36357	112.4	1395	2.121E-05	0.0038	3.302E-05	0.047
Channel	228	7.6	1014	1.176E-04	0.0004	3.720E-05	0.053
Combustor	347	11.0	205	2.262E-04	0.0050	5.442E-05	0.093
Vaneless Channel upstream of IGV	52	4.2	3902	3.707E-06	0.0001	5.375E-05	0.092
IGV	4420	39.2	2831	3.233E-05	0.0012	4.931E-05	0.085
Vaneless Channel upstream of Rotor Tur	9522	57.5	3490	2.576E-06	0.0013	4.495E-05	0.077
Turbine Casing	1782	7.6	1387	9.425E-06	0.0004	4.258E-05	0.073
Turbine Rotor	7074	49.6	1307	1.737E-05	0.0028	4.258E-05	0.073
Inter Disk Rear Cavities	10463	37.2	1024	1.885E-05	0.0020	3.832E-05	0.055
External Surface	#	#	10	3.330E-04	#	#	#
Stator Temperature (K)	990		Heat Transfer Rotor - Compressor (W)				9.79
Rotor Temperature (K)	769	or g/h	Heat Transfer Rotor - Turbine (W)				-7.51
Fuel Mass Flow Rate (kg/s)	2.76E-06	9.93	Compressor mechanical Power (W)				21.49
Inlet Combustor Temperature (K)	925		Turbine mechanical Power (W)				24.36
Specific Fuel Consumption (kg/J)	9.61E-07		Net Power (W)				2.87

Appendix 4

Performance for $T_{comb} = 1700K$

	Reynolds Number	Nusselt Number	h (W/m ² K)	S (m ²)	L (m)	Dynam. Viscosity	Th. Cond. (W/m/K)
	#	#	#	#	#	#	#
Inter Disk Front Cavity	9872	36.2	1016	9.425E-06	0.0020	3.917E-05	0.056
Compressor Rotor	13859	69.4	1512	1.737E-05	0.0015	2.277E-05	0.033
Vaneless Channel upstream of Diffuser	32809	106.8	2476	8.105E-06	0.0018	2.909E-05	0.042
Diffuser	34984	110.3	1392	2.121E-05	0.0038	3.347E-05	0.048
Channel	225	7.6	1032	1.176E-04	0.0004	3.786E-05	0.054
Combustor	313	10.4	202	2.262E-04	0.0050	5.631E-05	0.097
Vaneless Channel upstream of IGV	50	4.2	3973	3.707E-06	0.0001	5.559E-05	0.095
IGV	4191	38.2	2845	3.233E-05	0.0012	5.083E-05	0.087
Vaneless Channel upstream of Rotor Tur	9032	56.0	3496	2.576E-06	0.0013	4.618E-05	0.079
Turbine Casing	1706	7.6	1425	9.425E-06	0.0004	4.375E-05	0.075
Turbine Rotor	6605	47.9	1298	1.737E-05	0.0028	4.375E-05	0.075
Inter Disk Rear Cavities	9872	36.2	1016	1.885E-05	0.0020	3.917E-05	0.056
External Surface	#	#	10	3.330E-04	#	#	#
Stator Temperature (K)	1028			Heat Transfer Rotor - Compressor (W)			10.41
Rotor Temperature (K)	796	or g/h		Heat Transfer Rotor - Turbine (W)			-8.18
Fuel Mass Flow Rate (kg/s)	3.00E-06	10.81		Compressor mechanical Power (W)			21.49
Inlet Combustor Temperature (K)	958			Turbine mechanical Power (W)			25.48
Specific Fuel Consumption (kg/J)	7.52E-07			Net Power (W)			3.99

Performance for $T_{comb} = 1800K$

	Reynolds Number	Nusselt Number	h (W/m ² K)	S (m ²)	L (m)	Dynam. Viscosity	Th. Cond. (W/m/K)
	#	#	#	#	#	#	#
Inter Disk Front Cavity	9342	35.2	1010	9.425E-06	0.0020	4.000E-05	0.057
Compressor Rotor	13697	69.0	1512	1.737E-05	0.0015	2.290E-05	0.033
Vaneless Channel upstream of Diffuser	31968	105.4	2469	8.105E-06	0.0018	2.939E-05	0.042
Diffuser	33707	108.2	1389	2.121E-05	0.0038	3.391E-05	0.049
Channel	222	7.6	1049	1.176E-04	0.0004	3.849E-05	0.055
Combustor	285	9.9	198	2.262E-04	0.0050	5.814E-05	0.100
Vaneless Channel upstream of IGV	49	4.1	4041	3.707E-06	0.0001	5.736E-05	0.098
IGV	3986	37.2	2659	3.233E-05	0.0012	5.231E-05	0.090
Vaneless Channel upstream of Rotor Tur	8591	54.6	3500	2.576E-06	0.0013	4.735E-05	0.081
Turbine Casing	1639	7.6	1461	9.425E-06	0.0004	4.487E-05	0.077
Turbine Rotor	6296	46.8	1300	1.737E-05	0.0028	4.487E-05	0.077
Inter Disk Rear Cavities	9342	35.2	1010	1.885E-05	0.0020	4.000E-05	0.057
External Surface	#	#	10	3.330E-04	#	#	#
Stator Temperature (K)	1065			Heat Transfer Rotor - Compressor (W)			11.04
Rotor Temperature (K)	823	or g/h		Heat Transfer Rotor - Turbine (W)			-8.89
Fuel Mass Flow Rate (kg/s)	3.25E-06	11.70		Compressor mechanical Power (W)			21.49
Inlet Combustor Temperature (K)	991			Turbine mechanical Power (W)			26.61
Specific Fuel Consumption (kg/J)	6.35E-07			Net Power (W)			5.12

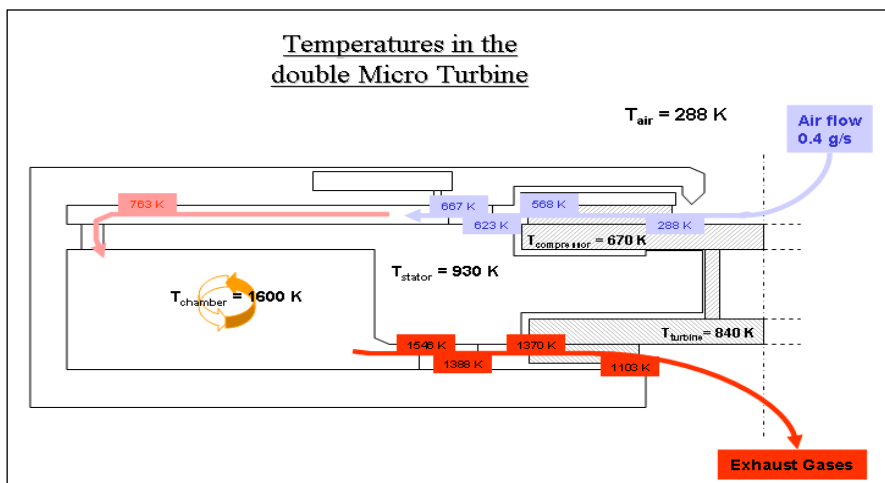
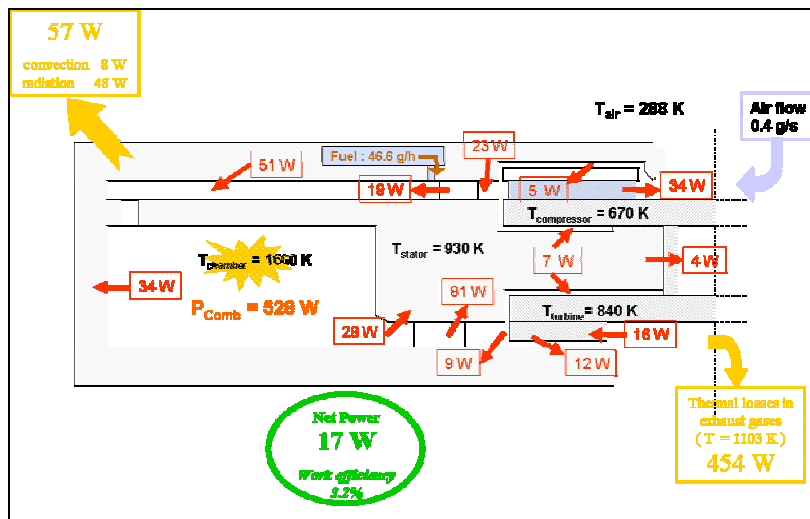
Appendix 5

Aerothermodynamics Conditions for the Double-Sized Micro-Turbine

		Compression Rate		3.53		
		Biot Number		0.036		
		Specific Heat Ratio for Burnt Gases		1.31		
Brayton - Joule Cycle	1->2	Compression				
	2->3	Combustion at constant Pressure				
	3->4	Expansion				
1	Static Pressure (Pa)	98660		356578		
	Total Pressure (Pa)	101325		357716		
	Static Temperature (K)	286		1600		
	Total Temperature (K)	288		1600		
	Static Mass per Unit Volume (kg/m ³)	1.201		0.775		
	Total Mass per Unit Volume (kg/m ³)	1.224		0.859		
2	Static Pressure (Pa)	354113		87191		
	Total Pressure (Pa)	357716		101325		
	Static Temperature (K)	717		1009		
	Total Temperature (K)	709		1043		
	Static Mass per Unit Volume (kg/m ³)	1.719		0.301		
	Total Mass per Unit Volume (kg/m ³)	1.756		0.338		
3 Combustion Chamber	Static Pressure (Pa)			87191		
	Total Pressure (Pa)			101325		
	Static Temperature (K)			1009		
	Total Temperature (K)			1043		
	Static Mass per Unit Volume (kg/m ³)			0.301		
	Total Mass per Unit Volume (kg/m ³)			0.338		
4	Static Pressure (Pa)			87191		
	Total Pressure (Pa)			101325		
	Static Temperature (K)			1009		
	Total Temperature (K)			1043		
	Static Mass per Unit Volume (kg/m ³)			0.301		
	Total Mass per Unit Volume (kg/m ³)			0.338		
Rotor Compressor Inlet (1)	Alpha (deg)	90		Static P (Pa)	98660	
	Beta (deg)	75.2		Total P (Pa)	101325	
	Merid. Mach Nbr	0.20	Meridional Speed	66	Static T (K)	286
	Tangential Mach Nbr	0	Tangential Speed	0	Total T (K)	288
	Relative Mach Nbr	0.76	Relative Speed	259	Static Rho (kg/m ³)	1.201
			Omega * R	250	Total Rho (kg/m ³)	1.224
	Mach Number	0.20	Speed (m/s)	66		
Rotor Compressor Exit	Alpha (deg)	3.8		Static P (Pa)	193705	
	Beta (deg)	67.8		Total P (Pa)	357716	
	Merid. Mach Nbr	0.06	Meridional Speed	29	Static T (K)	485
	Tangential Mach Nbr	0.97	Tangential Speed	430	Total T (K)	575
	Relative Mach Nbr	0.17	Relative Speed	76	Static Rho (kg/m ³)	1.390
			Omega * R	500	Total Rho (kg/m ³)	2.166
	Mach Number	0.98	Speed (m/s)	431		
Diffuser Inlet	Alpha (deg)	3.7		Static P (Pa)	238697	
	Beta (deg)	#		Total P (Pa)	357716	
	Merid. Mach Nbr	0.05	Meridional Speed	24	Static T (K)	574
	Tangential Mach Nbr	0.78	Tangential Speed	374	Total T (K)	639
	Relative Mach Nbr	#	Relative Speed	#	Static Rho (kg/m ³)	1.446
			Omega * R	#	Total Rho (kg/m ³)	1.949
	Mach Number	0.78	Speed (m/s)	374		
Diffuser Exit (2)	Alpha (deg)	18.7		Static P (Pa)	354113	
	Beta (deg)	#		Total P (Pa)	357716	
	Merid. Mach Nbr	0.03	Meridional Speed	17	Static T (K)	717
	Tangential Mach Nbr	0.09	Tangential Speed	51	Total T (K)	709
	Relative Mach Nbr	#	Relative Speed	#	Static Rho (kg/m ³)	1.719
			Omega * R	#	Total Rho (kg/m ³)	1.756
	Mach Number	0.10	Speed (m/s)	54		
IGV Inlet	Alpha (deg)	90		Static P (Pa)	355993	
	Beta (deg)	#		Total P (Pa)	357716	
	Merid. Mach Nbr	0.05	Meridional Speed	35	Static T (K)	1550
	Tangential Mach Nbr	0	Tangential Speed	0	Total T (K)	1550
	Relative Mach Nbr	#	Relative Speed	#	Static Rho (kg/m ³)	0.799
			Omega * R	#	Total Rho (kg/m ³)	0.803
	Mach Number	0.05	Speed (m/s)	35		
IGV Exit	Alpha (deg)	6.6		Static P (Pa)	240068	
	Beta (deg)	#		Total P (Pa)	357716	
	Merid. Mach Nbr	0.08	Meridional Speed	56	Static T (K)	1207
	Tangential Mach Nbr	0.72	Tangential Speed	488	Total T (K)	1325
	Relative Mach Nbr	#	Relative Speed	#	Static Rho (kg/m ³)	0.692
			Omega * R	#	Total Rho (kg/m ³)	0.939
	Mach Number	0.73	Speed (m/s)	491		
Rotor Turbine Inlet	Alpha (deg)	6.8		Static P (Pa)	229067	
	Beta (deg)	11.3		Total P (Pa)	357716	
	Merid. Mach Nbr	0.09	Meridional Speed	61	Static T (K)	1184
	Tangential Mach Nbr	0.77	Tangential Speed	512	Total T (K)	1313
	Relative Mach Nbr	0.09	Relative Speed	62	Static Rho (kg/m ³)	0.673
			Omega * R	500	Total Rho (kg/m ³)	0.948
	Mach Number	0.77	Speed (m/s)	516		
Rotor Turbine Exit (4)	Alpha (deg)	90		Static P (Pa)	87191	
	Beta (deg)	42.5		Total P (Pa)	101325	
	Merid. Mach Nbr	0.44	Meridional Speed	273	Static T (K)	1009
	Tangential Mach Nbr	0	Tangential Speed	0	Total T (K)	1043
	Relative Mach Nbr	0.60	Relative Speed	370	Static Rho (kg/m ³)	0.301
			Omega * R	250	Total Rho (kg/m ³)	0.338
	Mach Number	0.44	Speed (m/s)	273		

	Reynolds Number	Nusselt Number	h (W/m ² K)	S (m ²)	L (m)	Dynam. Viscosity	Th. Cond. (W/m/K)
	#	#	#	#	#	#	#
Inter Disk Front Cavity	20651	52.3	723	3.770E-05	0.0040	3.851E-05	0.055
Compressor Rotor	29292	100.9	1071	6.947E-05	0.0030	2.219E-05	0.032
Vaneless Channel upstream of Diffuser	74204	180.6	1773	3.242E-05	0.0036	2.770E-05	0.040
Diffuser	82998	169.9	995	8.483E-05	0.0077	3.155E-05	0.045
Channel	492	7.6	472	4.702E-04	0.0008	3.462E-05	0.050
Combustor	712	15.7	147	9.048E-04	0.0100	5.442E-05	0.093
Vaneless Channel upstream of IGV	103	6.0	2766	1.483E-05	0.0002	5.393E-05	0.092
IGV	9193	56.5	2068	1.293E-04	0.0023	5.000E-05	0.086
Vaneless Channel upstream of Rotor Tur	18979	81.2	2521	1.030E-05	0.0025	4.604E-05	0.079
Turbine Casing	22887	89.2	1282	3.770E-05	0.0052	4.375E-05	0.075
Turbine Rotor	13321	68.0	921	6.947E-05	0.0055	4.375E-05	0.075
Inter Disk Rear Cavities	20651	52.3	723	7.540E-05	0.0040	3.851E-05	0.055
External Surface	#	#	10	1.332E-03	#	#	#
Stator Temperature (K)	972					Heat Transfer Rotor - Compressor (W)	29.20
Rotor Temperature (K)	777	or g/h				Heat Transfer Rotor - Turbine (W)	-27.74
Fuel Mass Flow Rate (kg/s)	1.18E-05	42.32				Compressor mechanical Power (W)	85.96
Inlet Combustor Temperature (K)	808					Turbine mechanical Power (W)	105.43
Specific Fuel Consumption (kg/J)	6.04E-07					Net Power (W)	19.48

Table 11: Powers of the Double-Sized Micro-Turbine



Heat Transfer and Temperature Repartition in the Microturbine ($\Phi = 2$ cm)